Bulletin of the Seismological Society of America, Vol. 105, No. 2A, pp. 511–543, April 2015, doi: 10.1785/0120140093

Long-Term Time-Dependent Probabilities for the Third Uniform California Earthquake Rupture Forecast (UCERF3)

by Edward H. Field, Glenn P. Biasi, Peter Bird, Timothy E. Dawson, Karen R. Felzer, David D. Jackson, Kaj M. Johnson, Thomas H. Jordan, Christopher Madden, Andrew J. Michael, Kevin R. Milner, Morgan T. Page, Tom Parsons, Peter M. Powers, Bruce E. Shaw, Wayne R. Thatcher, Ray J. Weldon II, and Yuehua Zeng

Abstract The 2014 Working Group on California Earthquake Probabilities (WGCEP 2014) presents time-dependent earthquake probabilities for the third Uniform California Earthquake Rupture Forecast (UCERF3). Building on the UCERF3 time-independent model published previously, renewal models are utilized to represent elastic-rebound-implied probabilities. A new methodology has been developed that solves applicability issues in the previous approach for unsegmented models. The new methodology also supports magnitude-dependent aperiodicity and accounts for the historic open interval on faults that lack a date-of-last-event constraint. Epistemic uncertainties are represented with a logic tree, producing 5760 different forecasts. Results for a variety of evaluation metrics are presented, including logic-tree sensitivity analyses and comparisons to the previous model (UCERF2). For 30 yr $M \geq 6.7$ probabilities, the most significant changes from UCERF2 are a threefold increase on the Calaveras fault and a threefold decrease on the San Jacinto fault. Such changes are due mostly to differences in the time-independent models (e.g., fault-slip rates), with relaxation of segmentation and inclusion of multifault ruptures being particularly influential. In fact, some UCERF2 faults were simply too long to produce M 6.7 size events given the segmentation assumptions in that study. Probability model differences are also influential, with the implied gains (relative to a Poisson model) being generally higher in UCERF3. Accounting for the historic open interval is one reason. Another is an effective 27% increase in the total elastic-rebound-model weight. The exact factors influencing differences between UCERF2 and UCERF3, as well as the relative importance of logic-tree branches, vary throughout the region and depend on the evaluation metric of interest. For example, $M \geq 6.7$ probabilities may not be a good proxy for other hazard or loss measures. This sensitivity, coupled with the approximate nature of the model and known limitations, means the applicability of UCERF3 should be evaluated on a case-by-case basis.

Introduction

This study provides time-dependent, elastic-rebound-motivated probabilities for the third Uniform California Earthquake Rupture Forecast (UCERF3). This model has been developed by the 2014 Working Group on California Earthquake Probabilities, referred to hereafter as WGCEP 2014, the results of which are represented by this and other publications cited below. As with the previous UCERF2 model (WGCEP, 2007, also published as Field *et al.*, 2009), the purpose of UCERF3 is to provide consensus estimates of the magnitude, location, and likelihood of potentially damaging earthquake ruptures in the greater California region (Fig. 1). As such, this earthquake rupture forecast constitutes one of the two main model components used in seismic-hazard and risk assessment (the other model provides ground-shaking estimates for each rupture). The time-dependent model presented here builds on the UCERF3 time-independent model, the latter being fully described in a previous report (Field *et al.*, 2013), including 20 appendixes that stand alone in terms of relevance beyond UCERF3. That document is referred to hereafter as the UCERF3-TI report (TI stands for time independent) and is also where further details on the motivation, history, participation, and review process for the overall UCERF3 project can be found. The UCERF3-TI main report (excluding appendixes) is also published as Field *et al.* (2014).

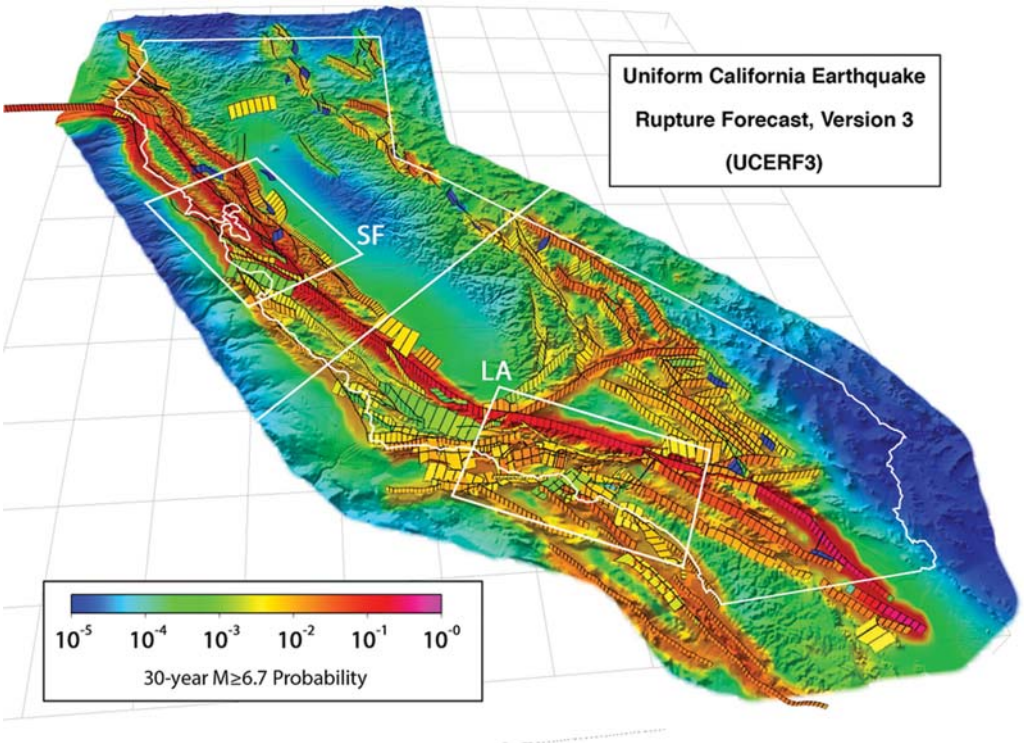

Figure 1. Three-dimensional perspective view of the third Uniform California Earthquake Rupture Forecast (UCERF3). The small black rectangular elements represent the 2606 fault subsections used in the forecast (for one of the two fault models, FM3.1). The along-strike length of each subsection is equal to half the down-dip width, and supraseismogenic ruptures are defined as two or more contiguous subsections. Colors depict the mean participation probability, the likelihood that each point will experience one or more $M \geq 6.7$ earthquakes in the 30 years following 2014 (for which participation means that some point on the rupture surface is within about 5 km). The entire colored area represents the UCERF model region, which comprises California and a buffer zone (referred to as All CA in the text). The white boxes define the San Francisco (SF) Bay and Los Angeles (LA) regions, respectively, and the white line crossing the state is our definition of northern versus southern California (referred to as N. CA and S. CA, respectively, in the text). The influence of the Cascadia megathrust is not shown on this map.

Every forecast model is an approximation of the natural system, and we acknowledge that earthquakes exhibit behavioral complexities that are beyond our current understanding. Given the infrequency of large damaging earthquakes, there may also be important features we have not yet observed, as many earthquakes continue to surprise us. Against this backdrop, the present study is an attempt to represent the influence of the Reid (1911) elastic-rebound theory, which posits rupture probabilities drop on a fault after experiencing a large rupture and then build back up as tectonic stresses reaccumulate with time. We understand there are other processes at work, the most obvious of which is spatiotemporal clustering (e.g., aftershock triggering). There might also be longer-term effects, such as mode switching (Dahmen *et al.*, 1998; Ben-Zion *et al.*, 1999; Zaliapin *et al.*, 2003; Ben-Zion, 2008) or super cycles (Grant and Sieh, 1994; Weldon *et al.*, 2004; Dolan *et al.*, 2007; Goldfinger *et al.*, 2013; Rockwell *et al.*, 2014; Schwartz *et al.*, 2014). We do not attempt to model these other processes here. We also acknowledge data limitations have prevented a definitive confirmation of Reid's elastic-rebound hypothesis, at least for large, damaging earthquakes. The model presented here therefore represents our best estimate of the elastic-rebound component of the system, under the assumption such behavior exists and can be meaningfully isolated from other time dependencies.

Similar to its predecessors, UCERF3 is composed of the four main model components shown in Figure 2. The fault model gives the physical geometry of the larger, known, and more active faults; the deformation model gives slip-rate and creep estimates for each fault section, as well as deformation rates off the modeled faults (if available); the earthquake rate model gives the long-term rate of all earthquakes throughout the region (at some level of discretization); and the earthquake probability model gives the likelihood that each event will occur during a specified time span, perhaps conditioned on additional information such as date of last event. Alternative versions of each component are defined in order to represent the epistemic uncertainties from incomplete knowledge of how the earthquake system works. Except where otherwise noted, all magnitudes referenced here as M represent moment magnitude.

The UCERF3 Time-Independent Model

The UCERF3 fault models, deformation models, and earthquake rate models collectively represent the complete time-independent model and are fully documented in the

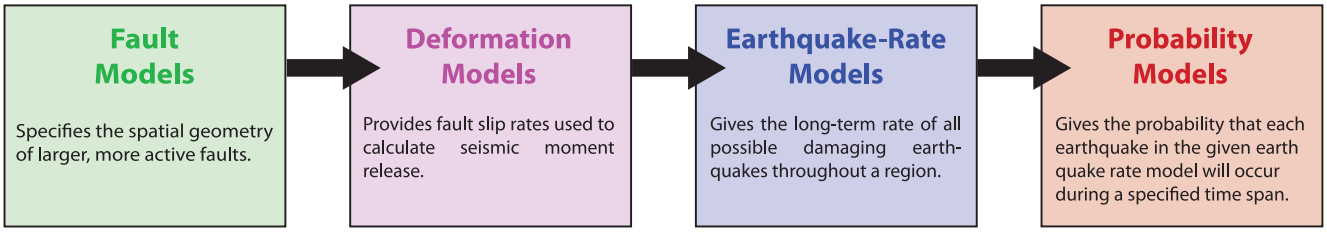

Figure 2. The four main model components used in the UCERF3 framework.

UCERF3-TI report (Field *et al.*, 2013). Two primary achievements for UCERF3-TI have been the relaxation of fault-segmentation assumptions and the inclusion of multifault ruptures, both identified as modeling limitations in the UCERF2 report. These were achieved using a system-level grand inversion, in which the rates of all earthquakes are solved for simultaneously from a variety of data constraints. The inverse problem is large and inherently underdetermined; therefore, a range of models was sampled using an efficient simulated annealing algorithm (appendix N of the UCERF3-TI report [Page *et al.*, 2013]; also published as Page *et al.*, 2014). This new approach succeeded in removing the apparent overprediction of M 6.5–7 earthquake rates in UCERF2 and enabled inclusion of the types of multifault ruptures seen in nature.

UCERF3 defines three types of ruptures: (1) supraseismogenic on-fault ruptures (modeled with the rectangular elements shown in Fig. 1); (2) subseismogenic on-fault ruptures; and (3) off-fault ruptures (not associated with explicitly modeled faults). The latter two are represented with a geographic grid of magnitude–frequency distributions and are therefore sometimes referred to together as "gridded seismicity." Supraseismogenic means the square root of the rupture area is greater than the average down-dip width of the fault.

Epistemic uncertainties in the time-independent model are represented using 1440 alternative logic-tree branches (Fig. 3), reflecting a considerable expansion relative to UCERF2. For example, three of the new deformation models are based on kinematically consistent inversions of geodetic and geologic data, which not only provide a wider range of fault-slip rates, but also values for faults that were previously excluded due to lack of geologic data. A detailed presentation of each logic-tree branch is given in the UCERF3-TI report; here, we quantify which are most influential in terms of the various hazard metrics introduced below. The Figure 3 caption also gives a brief explanation of each branch.

The consensus of the 2014 Working Group is that UCERF3-TI represents a significant improvement over UCERF2. However, as described in the UCERF3-TI report, the model is still only an approximation of the natural system, and there may be areas where additional site-specific analyses are in order.

The UCERF3 Time-Dependent Model

This study addresses the fourth model component shown in Figure 2, the time-dependent model. In particular, we use renewal models to quantify the earthquake probabilities implied by elastic-rebound theory. Renewal models have been used for this purpose by all previous WGCEPs (1988, 1990, 1995, 2003, and 2007), with methodological improvements being made in each successive effort (e.g., see Field, 2007, for a review of those through WGCEP 2003).

In the context of UCERF2, WGCEP (2007) noted a self-consistency problem with their algorithm for computing elastic-rebound-based earthquake probabilities. In particular, Monte Carlo simulations revealed the following: (1) the distribution of recurrence intervals produced by the model were not equal to that assumed in the first place; (2) the simulated rates of events were biased high compared to those imposed; and (3) the final segment probabilities, aggregated from rupture probabilities, were not the same as those computed elsewhere in the algorithm (i.e., from the mean recurrence interval and time since the last event). For completely segmented models (WGCEP 1988 and 1990), where earthquakes always rupture the exact same stretch of fault with zero overlap among neighboring events, these issues are nonexistent. For segmented models that allow both single and multisegment ruptures (WGCEP 1995, 2003, and 2007), these issues have a minor influence on results compared to overall uncertainties. This, together with the lack of an alternative, is why the former elastic-rebound algorithm was accepted as the best available science in UCERF2. Unfortunately, these self-consistency problems worsen as segmentation assumptions are relaxed, so they needed to be addressed in UCERF3.

For UCERF3, segmentation has been relaxed by subdividing the main fault sections into many more, shorter-length subsections (Fig. 1) and by including ruptures on every contiguous set of subsections that pass some plausibility criteria (appendix T of the UCERF3-TI report by Milner *et al.*, 2013). The result is a much larger set of possible ruptures, with many more overlapping possibilities at each point in the fault system. For example, UCERF2 had only six different size ruptures passing through the Peninsula section of the San Andreas fault (when measured by area, and for the segmented model, which was given 90% weight), whereas UCERF3 has more than 49,000.

Using Monte Carlo simulations, Field (2015) has quantified how the removal of segmentation in UCERF3 exacerbates the self-consistency issues associated with the elastic-rebound probability calculations used in UCERF2. That study also presents a new, alternative approach that is less biased, more self-consistent, and in general agreement

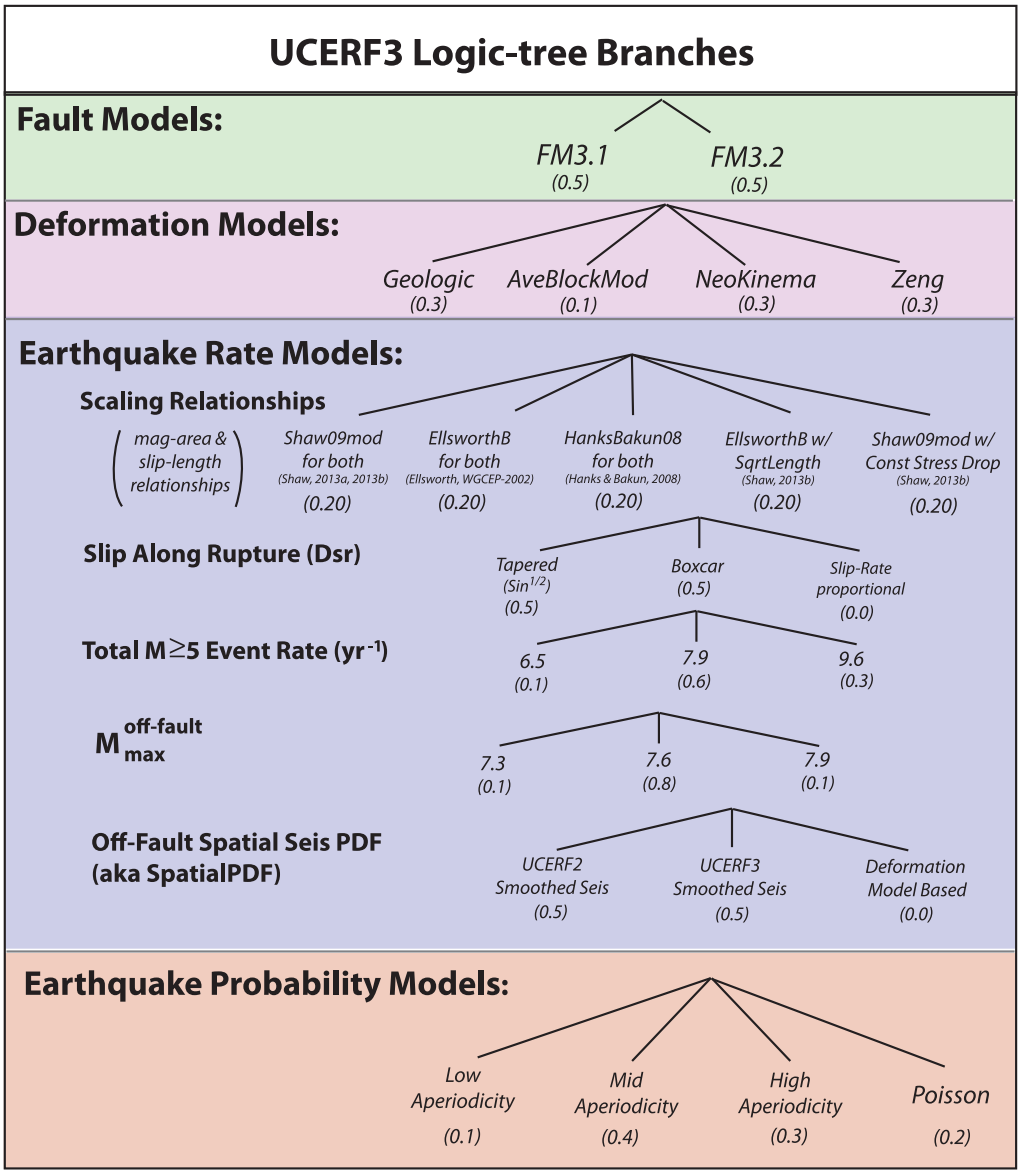

Figure 3. UCERF3 logic-tree branches, with weights given in parentheses. The branches are organized by the basic model components in Figure 2: fault models (green), deformation models (light purple), earthquake rate models (blue), and probability models (pink). UCERF3 has a total of 5760 logic-tree branches. The fault models represent alternative representations for several fault sections. The deformation models provide alternative fault-slip rate estimates, as well as the degree of aseismicity on each fault section. The scaling relationships are used to compute rupture magnitudes (from the area) and to define the mean slip for each rupture. The slip-along rupture models define the distribution of slip along strike (when averaged over many rupture occurrences). Total $M \geq 5$ event rate specifies the total yearly rate of events throughout the region, $\mathbf{M}_{\max}^{\text{off-fault}}$ represents the largest magnitude for events occurring off the modeled faults, and Off-Fault Spatial Seis PDF specifies how the off-fault seismicity rates vary across the region. The probability model options are discussed in the text and in Table 1. More details on all but the probability model branches can be found in the UCERF3-TI report (Field *et al.*, 2014).

with the elastic-rebound predictability implied by physics-based earthquake simulators. Given these and others advantages discussed in the Methodology section below, this new algorithm has been adopted for use in UCERF3.

Forthcoming Spatiotemporal Component and Operational Earthquake Forecasting

An important goal of UCERF3 has been the inclusion of spatiotemporal clustering to model aftershocks and triggered events, the practical importance of which was exemplified by the 2011 M 6.3 Christchurch, New Zealand, earthquake (e.g., Kaiser *et al.*, 2012). Ultimately, this version of UCERF3 could form the basis of an operational earthquake forecast for California, which by definition would include both authoritative, real-time forecasts and official protocols for communicating implications to the public (Jordan and Jones, 2010; Jordan *et al.*, 2011). Operational earthquake forecasting (OEF) is now listed as one of the strategic-action priorities of the U.S. Geological Survey (USGS), with a goal of providing

"effective situational awareness" to emergency managers during hazardous events (Holmes *et al.*, 2013, pp. 32–33).

A prototype spatiotemporal clustering component has been implemented based on the epidemic-type aftershocks sequence (ETAS) model (Ogata, 1988). The primary challenge has been to merge ETAS, which is a point-process model, into the finite-fault framework of UCERF3. Preliminary studies, in which the spatiotemporal algorithm was applied to UCERF2, identified two significant issues (Field, 2011, 2012). First, the underlying time-independent model needs to be more consistent with a Gutenberg–Richter distribution over aftershock-zone-size areas, as the strongly characteristic magnitude–frequency distributions in UCERF2 lead to runaway (never-ending) sequences. The inversion approach of UCERF3 appears to have at least mitigated this problem by including multifault ruptures and imposing a regional Gutenberg–Richter constraint. Second, spatiotemporal models based on observed triggering statistics require some form of elastic relaxation, otherwise a large triggered event is more likely to rerupture the exact same mainshock surface rather than an adjacent or separate fault, at least more so than is seen in nature. The elastic-rebound methodology presented here represents a promising solution to this problem, so further development of the spatiotemporal component has awaited its completion. However, full operationalization of UCERF3 will require solving other challenges as well, such as quantifying and dealing with network data quality issues in real time and distilling results into manageable and appropriate forms for different potential user groups.

Empirical Model

Both UCERF2 (WGCEP, 2007) and the previous model (WGCEP, 2003) included a so-called empirical model among the time-dependent options. The rationale for this was inferred from differences between more recent (post-1906 or later) and longer-term seismicity rates (post-1850). For example, WGCEP (2003) inferred an approximate 50% rate reduction in the San Francisco Bay area, which they suspected might have resulted from a stress shadow (Harris and Simpson, 1998) cast by the great 1906 earthquake. However, the stress-change models considered by WGCEP (2003) had difficulty producing this behavior, which motivated them to create the empirical rate-change model. Felzer (2007) developed a statewide version of this model for UCERF2 and found recent rate reductions in every area of California that had adequate data. In particular, the rate reduction for Los Angeles was about equal to that in San Francisco, calling into question the stress shadow interpretation. Although WGCEP (2007) confessed to lacking a preferred physical interpretation, they nevertheless applied the model in UCERF2 with a 30% branch weight. In this empirical model, the long-term rate of each fault-based rupture was reduced by the inferred rate reduction before computing a Poisson probability.

The empirical model has been updated for UCERF3 (Felzer, 2013; appendix Q of the UCERF3-TI report), with more attention being placed on possible artifacts due to data limitations and inadequate aftershock declustering. Statistically significant rate reductions are now found in only three, relatively small regions (around San Francisco, Santa Barbara, and the Imperial Valley). The physical cause remains elusive, and it is possible that the reductions are artifacts of some data limitation. Furthermore, it is possible that the time-dependent components in UCERF3 might produce such anomalies. Consequently, there was virtually no support within the present working group for including an empirical model in UCERF3, at least not until the forthcoming spatiotemporal component is shown to be inconsistent with the observations. A further complication is that any empirical model should probably depend on the forecast duration, which has not yet been fully considered. Given the alternative values of the total $M \geq 5$ event rate (logic-tree branch in Fig. 3), UCERF3 is consistent with recent seismicity rates, at least on a statewide basis (Felzer, 2013).

Methodology

We utilize a new procedure for computing elastic-rebound-based earthquake probabilities that largely solves the self-consistency and bias issues noted in the Introduction. Full details are given by Field (2015), including a comparison to the previous methodology, an analysis of what current physics-based earthquake simulators imply regarding elastic-rebound predictability, and Monte Carlo simulation tests of the new algorithm. We summarize implementation details here, including how to handle the fact that we lack date-of-last-event data on most faults. As with previous WGCEPs, the methodology is applicable only to large, fault-based ruptures and is therefore not applied to the gridded-seismicity sources.

The new approach, like its predecessor, assumes the availability of a long-term earthquake-rate model, which gives the frequency of all possible supraseismogenic ruptures on a fault or fault system, where the latter is represented by some number of fault subsections (or segments, as the case may be). Figure 1 shows the 2606 subsections for one of the two UCERF3 fault models. From this long-term rate model, the frequency of supraseismogenic events on each subsection can be computed as

$$f_s = \sum_{r=1}^{R} G_{sr} f_r, \tag{1}$$

in which f_s is the frequency of the sth subsection, f_r is the long-term rate of the rth rupture, and the matrix G_{sr} indicates which subsections are utilized by each rupture (values are 1 or 0). The mean recurrence interval of each subsection (μ_s) is then computed as

$$\mu_s = \frac{1}{f_s}. \tag{2}$$

Aftershocks are included in these rates, although this is not very important with respect to the implied probability gains

discussed below because these constitute only 3% of the moment rate for supraseismogenic events in UCERF3-TI.

The previous approach (WGCEP, 2003, 2007) involves computing a conditional probability for each subsection using this recurrence interval (μ_s), the time since the last event on the subsection (T_s), and an assumed aperiodicity (α, equal to the standard deviation of recurrence intervals divided by the mean, and sometimes referred to as the coefficient of variation). The Brownian passage time (BPT) renewal model (Matthews *et al.*, 2002) was used for the calculations, although results are nearly identical for a lognormal distribution (as applied in WGCEP 1988, 1990, and 1995). The probability for each rupture was then computed by aggregating the associated subsection probabilities (essentially multiplying the long-term rupture rate by a weighted average of the subsection probability gains).

To eliminate the self-consistency issues noted above, the new approach averages subsection recurrence intervals and dates of last event, rather than subsection probabilities (Field, 2015). Specifically, we first assume a given rupture will be the next event to occur, and then compute the expected recurrence interval as a weighted average of the long-term recurrence intervals of the subsections involved:

$$\mu_r^{cond} = \frac{\sum \mu_s A_s}{\sum A_s}, \tag{3}$$

in which the weights are subsection area (A_s) and the sums are only over the subsections utilized by the rth rupture (matrix G_{sr} is implicit here). We weight by area to be consistent with the physics-based simulator analysis (Field, 2015), although this weighting is not very influential because subsection areas are fairly uniform. The superscript *cond* indicates the recurrence interval is conditioned on the assumption that the rupture will be the next event to occur. Because of the existence of many overlapping rupture possibilities (e.g., with slightly different endpoints), these conditional recurrence intervals are generally much lower than that implied by the long-term rate of each rupture ($\mu_r^{cond} \ll \mu_r = 1/f_r$). In fact, if the fault discretization were to become infinitesimally small, leading to an infinite number of overlapping rupture possibilities, the long-term rate of each specific rupture would approach zero (meaning infinite recurrence interval). The conditional recurrence interval, on the other hand, represents what we would expect if the given rupture was the only event to occur along that stretch of fault.

Similarly, we also define an average, normalized time since the last event for the rth rupture as

$$\eta_r = \frac{\sum (T_s/\mu_s) A_s}{\sum A_s}, \tag{4}$$

in which T_s is the elapsed time on the sth subsection (which may vary between subsections in an unsegmented model), and the sums are, again, only over the subsections utilized by the rth rupture.

The renewal model probabilities depend on three parameters: (1) the time since the last event normalized by the mean recurrence interval ($\eta = T/\mu$); (2) the forecast duration (ΔT) normalized by the mean ($\Delta T/\mu$); and (3) the assumed aperiodicity (α). We therefore have all the information needed to compute the conditional BPT probability for a given rupture, which we write as P_r^{BPT}. This probability is conditional in both the traditional sense (that there has been a specified period of time since the last event) and in the sense that the rth rupture is assumed to be the next event to occur.

We now account for the fact that we do not know which of the many overlapping rupture possibilities will occur next. To do so, we multiply by the ratio of the conditional rupture recurrence interval to the long-term recurrence interval (μ_r^{cond}/μ_r) as proxy for probability that the rth rupture is chosen, given an occurrence of one of the overlapping ruptures:

$$P_r^{\mathrm{U3}} = P_r^{\mathrm{BPT}} \left[\frac{\mu_r^{cond}}{\mu_r} \right]. \tag{5}$$

In words, P_r^{BPT} is the probability of having the rth rupture in the given time span, conditioned on the fact that it will be the next event to occur, and $[\mu_r^{cond}/\mu_r]$ represents the relative likelihood of selecting the rth rupture given an occurrence of one the overlapping possibilities (the term in brackets is equal to the long-term rate of the rth rupture divided by a measure of the total rate of events along that stretch of fault). The superscript U3 indicates this approach was developed and adopted for UCERF3. Field (2015) discusses how equation (5) can also be viewed as an inhomogeneous Poisson process, in which the long-term rupture rate ($1/\mu_r$) is multiplied by a time-varying probability gain.

This new methodology is not perfect. For example, there are alternative approaches for averaging renewal-model parameters over the rupture subsections (Field, 2015). Fortunately, this is a relatively minor issue, at least in comparison to other epistemic uncertainties, as will be quantified below. Another issue is that Monte Carlo simulations overpredict the long-term rate of ruptures by about 10%. This bias is not unique to any particular ruptures or subsections, implying a system-wide correction could be made if so desired. Nevertheless, having to make any such correction is admittedly inelegant.

Recall that we are using simple point-process renewal models to represent the elastic-rebound component of the system. Specifically, we model each rupture as a separate renewal process, but where the model parameters are highly correlated due to overlapping ruptures. Given the acknowledged complexity of the real earthquake system, it is not clear that any such simplification should be perfectly unbiased. Furthermore, the 10% value is small compared to overall epistemic uncertainties, as will be quantified below, and is less than a 20% overprediction found when the UCERF2 elastic-rebound methodology is applied to UCERF3 (Field, 2015). This reduced bias, coupled with the greater self-consistency and agreement with physics-based simulators noted previously, led the current working group to adopt the new methodology as the best available option for representing elastic rebound in UCERF3.

Unknown Time since the Last Event and Historic Open Intervals

The methodology outlined above assumes knowledge of the date of the last event on each subsection, which is unavailable for most California faults. It also does not consider the historic open interval T_H, defined as the period of time over which we know an event has not occurred (i.e., since record keeping began).

To address this, let $f(t)$ be the probability density function (PDF) of recurrence intervals for a given renewal model. If the time since the last event is known only to be greater than T_H, then the probability of having an event over forecast duration (ΔT) is computed as (Field and Jordan, 2015)

$$\frac{\Delta T - \int_{T_H}^{T_H+\Delta T} F(T)dT}{\int_{T_H}^{\infty}[1-F(T)]dT}, \tag{6}$$

in which $F(T)$ is the cumulative distribution ($F(T) = \int_0^T f(t)dt$). We use this equation to compute P_r^{BPT} when the date of the last event is unavailable on all subsections of the rupture.

Mixture of Known and Unknown Time since Last Event

The situation is more complicated when we know the date of the last event on some subsections but not others. The PDF for the time since the last event $p(\tau)$, conditioned on the fact that it is greater than T_H, is given as (Field and Jordan, 2015)

$$p(\tau|\tau \geq T_H) = \frac{1-F(\tau)}{\int_{T_H}^{\infty}[1-F(t)]dt}. \tag{7}$$

In principle, we could aggregate such PDFs over all relevant subsections to get a joint probability for the date of the last event. However, each subsection can have a different $p(\tau)$ due to variations in subsection recurrence intervals (μ_s). Another problem is the recurrence interval distribution at a point on a fault, or subsection, does not generally agree with typical renewal models, nor should we expect them to (Field, 2015). For example, very short recurrence intervals can occur due to overlap among ruptures that occur on adjacent parts of a fault; this, by the way, produces the self-consistency problem noted with the UCERF2 elastic-rebound methodology. Therefore, we cannot safely assume a general form for $f(t)$ on fault subsections, at least not as safely as the assumption with respect to the conditional ruptures described above. A final issue is correlation in the date of last event among subsections, as the most recent rupture generally involves at least a few subsections. These complications necessitate simplifying assumptions.

The approach taken here is as follows. First, let η^k represent the average normalized time since the last event when known (again, weighted by subsection area for consistency). Next, we write the PDF for the subsection-averaged normalized time since the last event with unknown η^u conditioned on the recurrence interval being greater than T_H, as

$$p(\eta^u|\eta^u \geq T_H/\mu^u) = \frac{1-F(\tau)}{\int_{T_H/\mu^u}^{\infty}[1-F(t)]dt}. \tag{8}$$

This is the same as equation (7), except the distribution and forecast duration are normalized by the conditional recurrence interval where unknown (μ^u, which is computed exactly as μ_r^{cond}, but only over those sections where date of the last event is unknown).

Each candidate value of η^u (from equation 8) is combined with the known η^k to get a total, candidate normalized time since last event for the rupture:

$$\eta_r' = \frac{A^u\eta^u + A^k\eta^k}{A^u + A^k}, \tag{9}$$

in which A^u and A^k are the total sections areas where unknown and known, respectively. The total probability theorem is then used to compute the final conditional probability for the rupture as

$$\int_{T_H/\mu^u}^{\infty} p(\eta^u|\eta^u \geq T_H/\mu^u)P_r^{BPT}(\eta_r', \Delta T/\mu_r)d\eta^u. \tag{10}$$

The first term represents the probability for the candidate value of η^u (from equation 8), $P_r^{BPT}(\eta_r', \Delta T/\mu_r)$ is the conditional rupture probability computed from the combined normalized time since last event (η_r'), and considering T_H, and the integral is over all possible values of η^u (computed numerically). This formulation reverts to the simpler cases (above) when either the date of the last event is known on all fault sections or known on none of them.

Implementation Details

Aperiodicity Values and Probability Model Weights

One advantage of the new probability calculation is the ability to apply magnitude-dependent aperiodicity. As discussed by Field (2015), a decrease in aperiodicity with magnitude is both implied by current physics-based simulators and physically appealing in that smaller events are presumably more influenced by evolving stress heterogeneities, and less likely to be stress resetting events, than are larger earthquakes. Table 1 lists three sets of aperiodicity values based on those tested by Field (2015), which we adopt as alternative logic-tree branches with weights as listed (also shown at the bottom of Fig. 3).

These aperiodicity values apply to conditional ruptures, as described above, whereas values implied for a point on a fault (e.g., in a paleoseismic trench) are considerably larger. For example, the UCERF3 Monte Carlo simulations conducted by Field (2015) imply average subsection aperiodicity values (at points on faults) of 0.5, 0.6, and 0.7 for the low-, mid-, and high-range options listed in Table 1, respectively.

Table 1
Probability Model Options, Associated Aperiodicity Values, and Weights for the Third Uniform California Earthquake Rupture Forecast (UCERF3) Time-Dependent Model

	Aperiodicity				
Logic-Tree Branch	$M \leq 6.7$	$6.7 < M \leq 7.2$	$7.2 < M \leq 7.7$	$M > 7.7$	Weight
Low range	0.4	0.3	0.2	0.1	0.1
Mid range	0.5	0.4	0.3	0.2	0.4
High range	0.6	0.5	0.4	0.3	0.3
Poisson	1.0	1.0	1.0	1.0	0.2

For comparison, the values assumed for UCERF2 (at points) were 0.3, 0.5, and 0.7 (with weights of 0.2, 0.5, and 0.3, respectively). Therefore, aperiodicity values are actually more consistent between UCERF2 and UCERF3 than would appear from the values in Table 1.

We also include a Poisson (time-independent) model branch with a weight of 0.2 (Fig. 3 and Table 1). One reason for the Poisson branch is to acknowledge that some participants believe the elastic-rebound hypothesis remains unverified. Another is to hedge against one potentially problematic implication of this and all previous WGCEP elastic-rebound models: that there is a zero probability of having a supraseismogenic rupture occur immediately following and completely inside the rupture area of a larger event. It is conceivable, however, that dynamic-rupture effects could reload some internal, supraseismogenic-size portion of a mainshock surface, although this is apparently quite rare in that we know of no confirmed examples, and current physics-based simulators lack such rerupturing events (Field, 2015).

Adding a Poisson branch to allow some immediate reruptures is not technically correct, as logic-tree branches are intended to be mutually exclusive (nature adheres to either one or the other). A more correct approach would be to include such behavior in the elastic-rebound model itself, but we currently lack a justifiable means of doing so.

Another question is whether branch weights should vary among faults. For example, it is possible that less active, more poorly developed faults have greater aperiodicity or are better approximated by a Poisson model. Fortunately, this is not a first-order problem for UCERF3, because most of the lower slip-rate faults lack a date of the last event and have longer recurrence intervals, so their time-dependent probabilities are close to those of a Poisson process anyway.

All of these issues were discussed at length at a review meeting for the UCERF3 time-dependent model (23–24 January 2014), and the final values and branch weights in Table 1 reflect results from an informal poll taken among those in attendance (including members of the participatory Scientific Review Panel). Such issues should nevertheless serve as a reminder that the model is an approximation of the system, based on expert opinion, and that alternative weights might be appropriate in some applications, as discussed more below.

Date-of-Last-Event Data

Two categories of data are used for determining the date of the last event on faults in UCERF3: (1) historical earthquakes, where the extent of rupture is largely known from observation, and (2) prehistoric earthquakes, where the extent of rupture is inferred from geologic data. The UCERF3 fault sections that have a date-of-last-event constraint on one or more subsections are listed in Table 2, and the complete dataset with references can be obtained from sources in Data and Resources.

The historical date constraints listed in Table 2 were obtained largely from the surface-rupturing earthquakes compiled for the "Fault Activity Map of California" by Jennings and Bryant (2010). Only ruptures that were deemed supraseismogenic have been included, leaving out, for example, the 1980 M 5.8 Greenville earthquake. For historic earthquakes that did not produce surface rupture (e.g., 1933 Long Beach), the lateral extent was inferred from seismological studies. Subsections that have a historical date constraint are labeled with the earthquake name in Figure 4.

Twenty-five paleoseismic earthquakes are included in the date-of-last-event dataset, with associated fault sections being listed as "Paleo" under data type in Table 2. Paleoseismic constraints are more difficult to interpret in terms of defining the lateral rupture extent, because we can no longer assume they apply to an entire segment in our unsegmented model. Although one can imagine various sophisticated solutions to this problem, including something analogous to the stringing pearls analysis of Biasi and Weldon (2009), the approach taken here is relatively straightforward. For most cases (e.g., San Jacinto [Anza]), the extent of rupture was inferred from offset geologic features thought to have formed in the most recent earthquake, as compiled by Madden *et al.* (2013, appendix R of UCERF3-TI report).

Interpretations for the remaining paleoseismic sites are more speculative. For those that have both timing and offset data, we assume the collocated and adjacent subsections ruptured (a total of three subsections, corresponding to an ~20 km length on vertical strike-slip faults). For cases in which the timing and slip data are located on different but adjacent subsections, the contiguous subsections with data, plus the adjacent subsections without data on either end, are linked to define the rupture length. Finally, for subsections

Table 2
Summary of UCERF3 Date of Last Event Data (Where Available)

Fault Section Name	Fraction Subsects w/ Data	Average Years Since	Ave Norm Time Since	Calendar Year	UCERF2 Calendar Year	Data Type
Burnt Mountain	0.33	22	0.02	1992	—	Hist
Calaveras (Central) 2011 CFM	0.40	30	0.25	1984*	1982*	Hist
Calaveras (North) 2011 CFM	0.14	274	0.75	1740	1775	Paleo
Calico–Hidalgo	0.22	1364	2.64	650	—	Paleo
Camp Rock 2011	0.50	22	0.02	1992	—	Hist
Cerro Prieto	1.00	80	0.99	1934	—	Hist
Compton	0.60	1289	0.68	725	—	Paleo
Elmore Ranch	0.33	27	0.10	1987	—	Hist
Elsinore (Glen Ivy) rev	0.25	104	0.87	1910	1910	Hist
Elsinore (Julian)	0.50	1226	0.72	788	807	Paleo
Elsinore (Temecula) rev	0.50	281	0.39	1732.5	1732	Paleo
Emerson–Copper Mountain 2011	0.45	22	0.02	1992	—	Hist
Eureka Peak	0.67	22	0.03	1992	—	Hist
Garlock (Central)	0.75	506	1.24	1545, 1490	1540	Paleo
Garlock (East)	0.63	524	1.09	1490	1000	Paleo
Garlock (West)	0.29	329	0.40	1685	1695	Paleo
Great Valley 13 (Coalinga)	1.00	31	0.02	1983	—	Hist
Green Valley 2011 CFM	0.43	399	2.15	1616	—	Paleo
Hayward (No) 2011 CFM	0.10	301	1.52	1713	1715	Paleo
Hayward (So) 2011 CFM	1.00	146	1.40	1868	1868	Hist
Hector Mine	1.00	15	0.01	1999	—	Hist
Hilton Creek 2011 CFM	0.75	34	0.05	1980	—	Hist
Homestead Valley 2011	0.67	22	0.02	1992	—	Hist
Imperial	1.00	48	0.96	1940, 1979	—	Hist
Incline Village 2011 CFM	1.00	564	0.20	1450	—	Paleo
Johnson Valley (North) 2011 rev	0.43	22	0.03	1992	—	Hist
Kickapoo	1.00	22	0.03	1992	—	Hist
Laguna Salada	0.33	122	0.42	1892	—	Hist
Lenwood–Lockhart–Old Woman Springs	0.09	1864	3.37	150	—	Paleo
Little Salmon (Offshore)	0.25	358	0.50	1656	—	Paleo
Little Salmon (Onshore)	1.00	358	0.88	1656	—	Paleo
Newport–Inglewood alt 1	0.22	81	0.12	1933	—	Hist
Newport–Inglewood alt 2	0.22	81	0.09	1933	—	Hist
Northridge	1.00	20	0.02	1994	—	Hist
Oceanic–West Huasna	0.23	11	0.02	2003	—	Hist
Owens Valley	1.00	142	0.31	1872	—	Hist
Panamint Valley	0.24	564	0.80	1450	—	Paleo
Pisgah–Bullion Mountain–Mesquite Lake	0.36	15	0.02	1999	—	Hist
Puente Hills	0.60	314	0.19	1700	—	Paleo
Puente Hills (Santa Fe Springs)	1.00	314	0.16	1700	—	Paleo
Rodgers Creek–Healdsburg 2011 CFM	0.21	269	1.11	1745	1758	Paleo
Rose Canyon	0.30	361	1.24	1653	—	Paleo
San Andreas (Big Bend)	1.00	157	0.77	1857	1857	Hist
San Andreas (Carrizo) rev	1.00	157	0.89	1857	1857	Hist
San Andreas (Cholame) rev	1.00	157	0.90	1857	1857	Hist
San Andreas (Coachella) rev	1.00	334	1.97	1680	1680	Paleo
San Andreas (Mojave North)	1.00	157	0.77	1857	1857	Hist
San Andreas (Mojave South)	1.00	157	2.34	1857	1857	Hist
San Andreas (North Branch Mill Creek)	0.17	334	0.23	1680	—	Paleo
San Andreas (North Coast) 2011 CFM	1.00	108	0.94	1906	1906	Hist
San Andreas (Offshore) 2011 CFM	1.00	108	1.02	1906	1906	Hist
San Andreas (Parkfield)	1.00	10	0.46	2004	2004	Hist
San Andreas (Peninsula) 2011 CFM	1.00	108	0.52	1906	1906	Hist
San Andreas (San Bernardino N)	1.00	202	1.43	1812	1812	Hist
San Andreas (San Bernardino S)	1.00	202	1.23	1812	1812	Hist
San Andreas (Santa Cruz Mountains) 2011 CFM	1.00	43	0.40	1989†	1906†	Hist
San Cayetano	0.50	354	0.38	1660	—	Paleo
San Gregorio (North) 2011 CFM	0.13	260	0.77	1754	—	Paleo
San Jacinto (Anza) rev	0.83	143	0.46	1918, 1800	1795	Both
San Jacinto (Borrego)	1.00	46	0.08	1968	1968	Hist

(*continued*)

Table 2 (*Continued*)

Fault Section Name	Fraction Subsects w/ Data	Average Years Since	Ave Norm Time Since	Calendar Year	UCERF2 Calendar Year	Data Type
San Jacinto (Clark) rev	1.00	214	0.45	1800	1540	Paleo
San Jacinto (Superstition Mountain)	0.40	474	1.43	1540	—	Paleo
Sierra Madre (San Fernando)	1.00	43	0.03	1971	—	Hist
Superstition Hills	1.00	27	0.10	1987	—	Hist
White Mountains	0.11	28	0.05	1986	—	Hist
White Wolf	1.00	62	0.06	1952	—	Hist
Whittier alt 1	0.13	1864	3.64	150	207	Paleo
Whittier alt 2	0.14	1864	2.07	150	207	Paleo

Fraction Subsects w/ Data gives the fraction of fault length covered, Average Years Since is relative to 2014, Average Norm Time Since is the average years since the event divided by the total long-term model rate, Calendar Year is the year of the event (with duplicates where there is more than one along the fault section), UCERF2 Calendar Year is the value applied in UCERF2 (blank if not treated as such), and Data Type indicates whether it is a historical event (Hist) or from paleoseismology (Paleo). This dataset is also available with references from sources in Data and Resources.

*The value of 1984 for UCERF3 represents the 1984 Morgan Hill earthquake, which only ruptured ~40% of the parent fault section, whereas the value of 1982 used in UCERF2 was the modal value from Working Group on California Earthquake Probabilities (WGCEP; 2003) and was applied to the entire segment in the previous models.

†This fault section was assumed to have ruptured in the 1989 Loma Prieta earthquake in UCERF3, whereas the last rupture was assumed to be 1906 in UCERF2.

where only timing is available (no offset data), we assume only that subsection was involved. All of these rules constitute lower-bound rupture-length estimates, meaning the influence on time dependence is reduced relative to the default historic open interval.

Table 2 indicates which of the fault sections were treated as time dependent in UCERF2 (in an elastic-rebound sense), with 38 being added in UCERF3. Table 3 lists those that were treated as time dependent in UCERF2 (by assuming a value) but lack any actual data constraint; they are treated here with the historic open interval.

Historic Open Interval

We use the year 1875 to define the historic open interval ($T_H = 2014 - 1875 = 139$ years). That is, for faults where we lack a date of the last event, we assume it is sometime prior to 1875. This value represents a compromise among

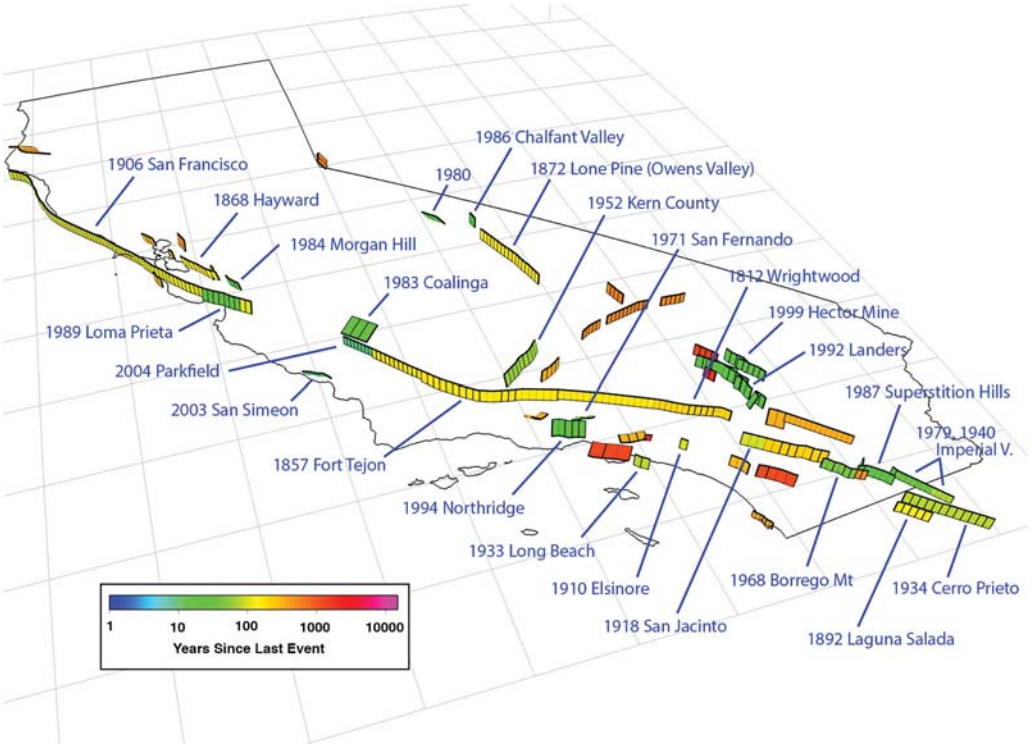

Figure 4. Fault subsections that have a historical date-of-last event, based on the earthquakes as labeled. The scale, years since last event, is relative to 2014.

Table 3
Fault Sections that Were Treated as Time Dependent in UCERF2 (in an Elastic-Rebound Sense), but that Currently Lack Any Type of Date-of-Last-Event Constraint (Previous Values were Assumed)

Fault Section Name	UCERF2 Calendar Year
Calaveras (South)	1899
Elsinore (Coyote Mountain)	1892
Elsinore (Glen Ivy stepover)	1910
San Andreas (San Gorgonio Pass–Garnet Hill)	1680
San Jacinto (Coyote Creek)	1892
San Jacinto (San Bernardino)	1769
San Jacinto (San Jacinto Valley) rev	1981

working-group members, with perspectives ranging from about 1850 to 1900. Fortunately, the sensitivity tests presented below imply that, while accounting for the historic open interval is important, the range of reasonable choices is not overly influential.

We understand there may be some post-1875 supraseismogenic events that remain unassociated with particular faults. Handling these properly would involve defining logic-tree branches and associated weights for every possible fault of origin. However, unless the event can be associated with only very few candidates, it is not likely to have an appreciable impact on average hazard estimates. Another question is whether the historic open interval should vary by fault. However, doing so significantly complicates the methodology (e.g., requiring some averaging of values over the subsections utilized by each rupture), so we have not attempted to do so here.

Results

Probability of What?

We are able to compute a variety of evaluation metrics with UCERF3, including probabilities for individual ruptures, different fault subsections, and aggregates for sets of faults or for different subregions within the state. We can also compute hazard curves and hazard maps, as utilized extensively in the UCERF3-TI report, as well as statewide loss estimates (e.g., Porter *et al.*, 2012). Results for a time-dependent model also depend on the start year and duration of the forecast, both of which are adjustable in UCERF3.

With more than 250,000 ruptures on each logic-tree branch, it is not feasible to present the probability of each in this report. Instead, we quantify the probability that each fault subsection will participate in one or more events of interest (e.g., $M \geq 6.7$), which, as discussed in the UCERF3-TI report, is a more relevant hazard metric anyway. Because there are more than 2600 subsections (the exact number depends on the chosen fault model), we show such probabilities in map form only. For tabulated values, we aggregate probabilities back onto the 350 main, or parent, fault sections.

We use a start year of 2014 for the UCERF3 results presented here. However, UCERF2 probabilities are based on a start year of 2007, in accordance with the value applied in that study. To make meaningful comparisons, we follow the WGCEP tradition of focusing on $M \geq 6.7$ probabilities for a 30 year forecast. Some other hazard-related metrics are also presented, however, and computer code exists for those who want to explore other possibilities (see Data and Resources).

All fault-based probabilities correspond to supraseismogenic ruptures. The contributions from subseismogenic ruptures and off-fault seismicity are included where appropriate, but only using a time-independent (Poisson) model. Except where noted, the contribution from aftershocks is included, which manifests as a 3% increase in long-term rates for supraseismogenic ruptures (as described in the UCERF-TI report); probabilities cited for UCERF2 here have also been corrected accordingly, whereas those listed in the original UCERF2 report do not include the 3% aftershock contribution.

The UCERF3 time-independent model has 1440 logic-tree branches. Adding the four probability model options (Fig. 3; Table 1) gives 5760 branches for the time-dependent model. Unless otherwise noted, results represent an average over the entire logic tree, weighted by the relative probability of each branch. To indicate epistemic uncertainties, we also tabulate minimum and maximum values among the logic-tree branches. An alternative would be to cite the 95% confidence bounds or any other percentile implied by the logic-tree branches (and weights). However, stating such confidence bounds would be misleading, as it assumes all viable models are represented on the logic tree, which we know is not the case. We therefore use minimum and maximum values as a measure of the epistemic uncertainty here but emphasize these are only within the context of our inevitably limited model.

Extensive tests have also been conducted to explore sensitivity to various calculation options, including different viable averaging approaches, alternative historic open intervals, and different assumptions with respect to the along-fault extent of date-of-last-event constraints. Only a representative subset of these analyses is presented here.

Subsection Probabilities

Figure 5a shows 30 yr, $M \geq 6.7$, branch-averaged probabilities for each UCERF3 fault subsection, together with the implied probability gain relative to Poisson (Fig. 5b), and the ratio with respect to UCERF2 for the faults used in both studies (Fig. 5c). Results for other magnitude thresholds and for a 5 year forecast are available from sources in Data and Resources.

It is important to understand the probability gains in Figure 5b represent an average over all ruptures, essentially weighted by the relative rate of each. Figure 5d shows the probability gains implied by using the average, long-term recurrence interval of each subsection (μ_s, including all supraseismogenic ruptures), together with the time since last event where known (T_s) and an assumed aperiodicity (α) of 0.3; this represents the result that would be obtained if each subsection ruptured only by itself. Figure 5d exhibits both

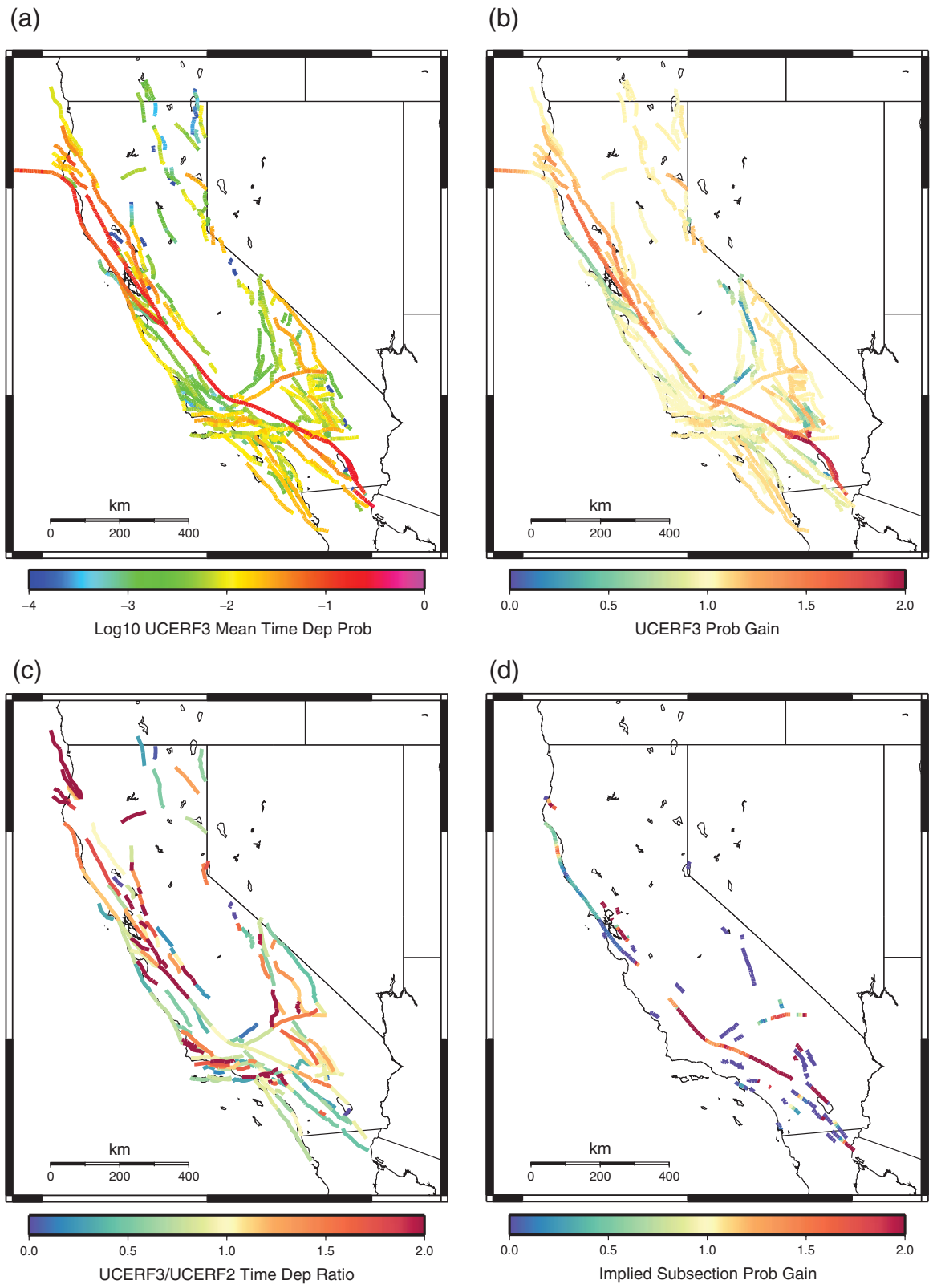

Figure 5. (a) Average $M \geq 6.7$ 30 yr subsection probabilities for all UCERF3 time-dependent model branches. (b) UCERF3 subsection probability gains (average time-dependent result divided by average of all time-independent/Poisson model branches). (c) Ratio of UCERF3 to UCERF2 probabilities for faults used in both studies, where UCERF3 subsection probabilities have been aggregated onto parent sections before taking the ratio. (d) Thirty-year subsection probabilities computed using average UCERF3 recurrence interval (including all supra-seismogenic ruptures), time since last event (where known), and an assumed aperiodicity of 0.3; the historic open interval is ignored (zero) in this plot. Only fault traces are shown in these plots.

Table 4

30 yr $M \geq 6.7$ UCERF3 Probabilities Aggregated by Parent Fault Section, Where the List Here Represents Sections that Have the 10 Lowest and 10 Highest Probability Gains

Fault Section Name	Fract SubSects with Data	Ave Years Since	Ave Norm Time Since	Mean	Min.	Max.	Pois	Gain
Kickapoo	1.00	22	0.03	9.07×10^{-04}	1.12×10^{-08}	1.60×10^{-02}	4.02×10^{-03}	0.22
Owens Valley	1.00	142	0.31	1.12×10^{-02}	2.01×10^{-04}	7.48×10^{-02}	3.92×10^{-02}	0.28
White Wolf	1.00	62	0.06	3.90×10^{-03}	6.76×10^{-05}	3.28×10^{-02}	1.22×10^{-02}	0.30
Homestead Valley 2011	0.67	22	0.02	3.04×10^{-03}	1.95×10^{-06}	2.45×10^{-02}	9.40×10^{-03}	0.31
Owens Valley Keough Hot Springs	0.00	—	—	6.04×10^{-03}	1.21×10^{-04}	4.04×10^{-02}	1.82×10^{-02}	0.37
Hector Mine	1.00	15	0.01	7.71×10^{-03}	4.72×10^{-05}	5.83×10^{-02}	1.36×10^{-02}	0.40
Great Valley 13 (Coalinga)	1.00	31	0.02	6.03×10^{-03}	2.32×10^{-04}	4.73×10^{-02}	1.67×10^{-02}	0.40
Hilton Creek 2011 CFM	0.75	34	0.05	1.25×10^{-02}	1.45×10^{-03}	7.28×10^{-02}	3.14×10^{-02}	0.41
Incline Village 2011 CFM	1.00	564	0.20	1.04×10^{-03}	0.00×10^{00}	6.03×10^{-03}	2.04×10^{-03}	0.51
Johnson Valley (North) 2011 rev	0.43	22	0.03	7.61×10^{-03}	9.48×10^{-05}	5.30×10^{-02}	1.37×10^{-02}	0.52
Hayward (No) 2011 CFM	0.10	301	1.52	1.82×10^{-01}	7.32×10^{-02}	3.41×10^{-01}	1.16×10^{-01}	1.57
San Gorgonio Pass	0.00	—	—	1.57×10^{-02}	2.07×10^{-03}	7.55×10^{-02}	9.67×10^{-03}	1.61
Brawley (Seismic Zone) alt 1	0.00	—	—	2.80×10^{-01}	9.05×10^{-02}	5.82×10^{-01}	1.73×10^{-01}	1.63
Imperial	1.00	48	0.96	2.60×10^{-01}	3.41×10^{-02}	5.96×10^{-01}	1.56×10^{-01}	1.70
Eureka Peak	0.67	22	0.03	2.23×10^{-04}	1.63×10^{-05}	1.58×10^{-03}	1.31×10^{-04}	1.75
San Andreas (San Bernardino S)	1.00	202	1.23	2.19×10^{-01}	4.41×10^{-02}	4.95×10^{-01}	1.22×10^{-01}	1.79
San Andreas (Coachella) rev	1.00	334	1.97	2.68×10^{-01}	6.68×10^{-02}	6.04×10^{-01}	1.43×10^{-01}	1.86
Brawley (Seismic Zone) alt 2	0.00	—	—	2.58×10^{-01}	4.33×10^{-02}	5.98×10^{-01}	1.36×10^{-01}	1.89
Joshua Tree (Seismicity)	0.00	—	—	1.50×10^{-03}	7.98×10^{-05}	1.40×10^{-02}	7.68×10^{-04}	1.94
San Andreas (San Gorgonio Pass-Garnet Hill)	0.00	—	—	2.10×10^{-01}	6.17×10^{-02}	5.10×10^{-01}	1.06×10^{-01}	1.97

Mean is the branch-averaged probability, Min. and Max. are the minimum and maximum among branches, Pois is the branch average time-independent result, and Gain is the ratio of Mean to Pois. Fract Subsects with Data represents the percentage of subsections that have a useable date of last event, Ave Years Since is the average where known (relative to 2014), and Ave Norm Time Since is the latter divided the long-term model recurrence interval (including all supraseismogenic events). These probabilities are computed as one minus the total probability that no $M \geq 6.7$ ruptures touch any part of the parent fault section. Results for all parent fault sections are available from sources in Data and Resources.

more extreme values and more spatial variability along faults, highlighting the strong influence of averaging in Figure 5b. The probability gain for any one rupture in UCERF3, however, is more like an along-fault average of those in Figure 5d (plus the influence of the historic open interval where data are lacking).

Figure 5c shows that, for most faults, the differences between UCERF2 and UCERF3 are greater than the UCERF3-implied probability gains (Fig. 5b). There are many potential explanations for the UCERF2 to UCERF3 changes, including (1) the many differences in the underlying long-term models (e.g., deformation model slip rates, scaling relationships, degree of segmentation); (2) change in the elastic-rebound probability calculation (e.g., methodological differences, magnitude-dependent aperiodicity, consideration of historic open interval); and (3) the fact that UCERF2 includes an empirical model component, which has been dropped in UCERF3 for reasons discussed in the Introduction. Although a complete accounting of the influence of each of these variables is beyond the present scope, general influences are revealed in the branch sensitivity tests presented below.

Parent Section Probabilities

Probabilities have also been aggregated onto the 350 parent fault sections (the total number between the two fault models). These represent participation probability, meaning the likelihood of an event occurring on any part of the parent fault section, even if the majority of the rupture surface is elsewhere. Although this definition is useful, especially when making comparisons to UCERF2, it can be deceptive. For example, probabilities depend on the total length of each parent section, which varies significantly throughout the fault model. Other potentially misleading cases are identified below.

Parent section probabilities for both 30 and 5 year forecasts, and for a variety of magnitude thresholds, are available from sources listed in Data and Resources. These include mean, minimum, and maximum values from the logic tree, as well as comparisons to UCERF2 where possible. For 30 yr $M \geq 6.7$ events, Table 4 lists the parent fault sections that have the 10 highest and 10 lowest probability gains, reflecting areas where the time dependence is particularly influential. All but one of the lowest gains are due to recent events, with the exception (Owens Valley Keough Hot Springs) representing a fault that mostly ruptures with another fault that did have a recent event (Owens Valley). This case exemplifies the effective averaging that occurs over neighboring fault sections.

The 10 highest probability gains in Table 4 are due to a relatively high normalized time since the last event and/or the historic open interval. The highest gain (1.97) is on the San Andreas (San Gorgonio Pass–Garnet Hill) fault section, which does not have a date-of-last-event constraint; the high gain is due to the historic open interval and a high rate of participation with San Andreas (Coachella) rev, the latter of which

Table 5
The Parent Fault Sections with the 10 Highest $M \geq 6.7$ 30 yr Probabilities

	Rank	Fault Section Name	Fract SubSects w/ Data	Ave Years Since	Ave Norm Time Since	Mean	U3 Gain	U2 Gain
UCERF3	1	Cerro Prieto*	1.00	80	0.99	0.30	1.05	—
	2	Mendocino*	0.00	—	—	0.28	1.33	—
	3	Brawley (Seismic Zone), alt 1 & alt 2*	0.00	—	—	0.27	1.76	—
	4	San Andreas (Coachella) rev	1.00	334	1.97	0.27	1.86	1.43
	5	San Andreas (Creeping Section) 2011 CFM	0.00	—	—	0.26	1.21	—
	6	Imperial	1.00	48	0.96	0.26	1.70	1.00
	7	Hayward (So) 2011 CFM	1.00	146	1.40	0.25	1.56	1.26
	8	San Andreas (San Bernardino N)	1.00	202	1.43	0.24	1.56	1.31
	9	San Andreas (Mojave South)	1.00	157	2.34	0.23	1.49	1.30
	10	Maacama 2011 CFM	0.00	—	—	0.23	1.54	0.94
UCERF2	1	San Andreas (Cholame) rev	—	—	—	0.30	1.40	1.29
	2	San Andreas (Coachella) rev	—	—	—	0.29	1.86	1.43
	3	Imperial	—	—	—	0.29	1.70	1.00
	4	San Andreas (Parkfield)	—	—	—	0.27	1.35	1.30
	5	San Andreas (Mojave South)	—	—	—	0.25	1.49	1.30
	6	San Andreas (Carrizo) rev	—	—	—	0.22	1.41	1.31
	7	San Andreas (Big Bend)	—	—	—	0.21	1.40	1.31
	8	San Andreas (Mojave North)	—	—	—	0.21	1.36	1.31
	9	San Andreas (San Bernardino N)	—	—	—	0.21	1.56	1.31
	10	Rodgers Creek–Healdsburg 2011 CFM	—	—	—	0.20	1.56	1.39

Mean is the mean probability and Gain is the mean divided by the Poisson-model mean, in which U3 Gain is the value for UCERF3 and U2 Gain is the value from UCERF2 for comparison if available. Fract Subsecs w/ Data represents the fraction of subsections that have a date-of-last-event constraint. UCERF2 results are listed at the bottom for comparison and are based on the start year of 2007 used in that study. Results for all parent fault sections are available from sources in Data and Resources.

*The names in the UCERF3 list were not included in the UCERF2 model.

constitutes the highest gain among faults with known date of last event. The exact same explanation (open interval and participation with San Andreas [Coachella] rev) applies to all other parent sections on the list that lack a date-of-last-event constraint. The high gains for Imperial and Eureka Peak, both of which have a date of last event, also result from high participation with San Andreas (Coachella) rev. Finally, San Andreas (San Bernardino S) has a high gain (1.79) due to a high normalized time since the last event, and Hayward (No) 2011 CFM has a high gain (1.57) due to both the historic open interval and a high normalized time since the last event (the latter defined on only a small portion of the parent section).

Two of the high-gain cases in Table 4 warrant further discussion, both because they recently ruptured. Joshua Tree (Seismicity) does not have a date of the last event because the 1992 M 6.1 Joshua Tree earthquake was deemed subseismogenic. Eureka Peak recently ruptured as a very early aftershock of the 1992 Landers earthquake sequence (Hough, 1994) but has a high gain due to it mostly participating with the San Andreas (Coachella) rev fault section. This high gain does not mean a high probability of occurrence, as the $M \geq 6.7$ 30 yr probability for Eureka Peak is just about 1 in 10,000.

Table 5 lists the top 10 parent fault sections in terms of total $M \geq 6.7$ 30 yr probabilities for both UCERF2 and UCERF3. Those ranked as first, second, and third for UCERF3 (Cerro Prieto, Mendocino, and Brawley [Seismic Zone], respectively), were not included as fault-based sources in UCERF2 but were treated as special, time-independent seismicity zones. Cerro Prieto has the top ranking due to a high long-term rate, as the probability gain is only 1.05. Mendocino and Brawley (Seismic Zone) make the list because of high gains, the reasons for which were discussed above (historic open interval and participation with San Andreas [Coachella] rev). In fact, high gains contribute significantly for all the other sections listed in Table 5. That the San Andreas (creeping section) 2011 CFM fault section makes the UCERF3 list might come as a surprise, given its high rate of creep and microseismicity. However, most of these events only slightly penetrate the creeping section from either the north or south; the probability of completely through-going ruptures is about 1 in 1000. Again, this serves as a reminder that such participation probabilities can be misleading. Maacama 2011 CFM has a large gain (1.54) due to a high long-term rate coupled with the historic open interval.

Aggregate Probabilities for Main Faults

Table 6 lists 30 yr $M \geq 6.7$ probabilities for several main faults, shown in Figure 6, each of which was treated as time dependent in UCERF2 (in an elastic-rebound sense). Logic-tree mean, minimum, and maximum values are listed, as well as probability gains with respect to Poisson, for both UCERF3 and UCERF2. Also listed is the ratio of UCERF3 to UCERF2 target moment rates in the time-independent models, giving an indication of long-term slip-rate changes. The moment rates are target values because neither model matched them exactly (due to trade-offs with paleoseismic event-rate constraints),

Table 6
Aggregate 30 yr $M \geq 6.7$ Probabilities (and Implied Gains Relative to a Time-Independent Model) for the Main Faults Considered by Previous WGCEPs

	UCERF3, from 2014				UCERF2, from 2007					
Main Fault Name	Mean	Min.	Max.	Gain	Mean	Min.	Max.	Gain	U3/U2 Mean	U3/U2 MoRate
South San Andreas*	0.53	0.17	0.93	1.45	0.60	0.23	0.94	1.22	0.87	0.88
North San Andreas†	0.33	0.01	0.73	0.96	0.21	0.06	0.40	0.87	1.56	0.84
Hayward–Rodgers Creek‡	0.32	0.14	0.54	1.52	0.32	0.12	0.68	1.34	1.01	1.24
Calaveras§	0.25	0.10	0.54	1.46	0.08	0.02	0.22	0.98	3.33	1.43
San Jacinto‖	0.09	0.00	0.35	0.83	0.32	0.14	0.55	1.02	0.29	0.77
Garlock#	0.08	0.00	0.37	1.16	0.06	0.03	0.13	1.06	1.34	0.85
Elsinore**	0.05	0.01	0.17	0.99	0.11	0.05	0.25	0.90	0.46	0.57

All probabilities have been rounded to the nearest percent, and UCERF2 results are listed for comparison. All results include aftershocks. Min. and Max. values represent the minimum and maximum among all logic-tree branches. U2/U3 MoRate is the ratio of UCERF3 to UCERF2 target moment rates.

*Fault Sections: San Andreas (Parkfield), San Andreas (Cholame) rev, San Andreas (Carrizo) rev, San Andreas (Big Bend), San Andreas (Mojave North), San Andreas (Mojave South), San Andreas (San Bernardino N), San Andreas (San Bernardino S), San Andreas (San Gorgonio Pass-Garnet Hill), San Andreas (North Branch Mill Creek), and San Andreas (Coachella) rev.

†Fault Sections: San Andreas (Offshore) 2011 CFM, San Andreas (North Coast) 2011 CFM, San Andreas (Peninsula) 2011 CFM, and San Andreas (Santa Cruz Mts) 2011 CFM.

‡Fault Sections: Rodgers Creek—Healdsburg 2011 CFM, Hayward (No) 2011 CFM, Hayward (So) 2011 CFM.

§Calaveras (North) 2011 CFM, Calaveras (Central) 2011 CFM, Calaveras (South) 2011 CFM.

‖San Jacinto (San Bernardino), San Jacinto (San Jacinto Valley) rev, San Jacinto (Stepovers Combined), San Jacinto (Anza) rev, San Jacinto (Clark) rev, San Jacinto (Coyote Creek), San Jacinto (Borrego), San Jacinto (Superstition Mountain).

#Garlock (East), Garlock (Central), Garlock (West).

**Whittier alt 1, Elsinore (Glen Ivy) rev, Elsinore (Stepovers Combined), Elsinore (Temecula) rev, Elsinore (Julian), Elsinore (Coyote Mountains).

but they are close enough to reflect overall slip-rate changes. Figure 7 shows the 30 year participation probability for each main fault as a function of magnitude threshold (cumulative magnitude–probability distributions).

South San Andreas. The South San Andreas exhibits the highest $M \geq 6.7$ probability among the main faults in UCERF3 (0.53), which is a little less than the UCERF2 value of 0.59. This change is consistent with a 12% reduction in the target moment rate (e.g., from Global Positioning System constraints), although this is one area where such targets are at odds with paleoseismic event-rate constraints. Furthermore, the probability gain increased from 1.23 to 1.45, suggesting the probability should have increased. Figure 7 reveals UCERF3 participation probabilities are actually higher than UCERF2 values at both lower and higher magnitudes ($M \leq 6.7$ and $M \geq 7.8$). Therefore, the reduction for $M \geq 6.7$ stems from moment rates going to other magnitudes, either in satisfying paleoseismic event-rate constraints or in removing the UCERF2 statewide overprediction of $M \sim 6.7$ event rates. Regardless, the differences between UCERF3 and UCERF2 values are generally quite small compared to overall uncertainties.

North San Andreas. The mean probability for $M \geq 6.7$ events on the North San Andreas has increased from 0.21 to 0.33, but results are generally consistent given the logic-tree minimum and maximum (e.g., 0.01 and 0.73, respectively, for UCERF3). Only a small fraction of this change can be attributed to the probability gain, which went from 0.87 to 0.96, and the target moment rate actually went down by 16%. The main cause is fault discretization, as can be inferred from Figure 7. In UCERF2, the North San Andreas was divided into only four segments, which ranged in length from ~70 to ~170 km, with mean characteristic magnitudes of 7.0 and 7.5, respectively (for single-segment ruptures). As such, there was no accommodation for seismogenic-thickness-size ruptures (i.e., $\sim 12 \times \sim 12$ km), except from an unsegmented model option that was only given a branch weight of 0.1 (and where most of the moment went into larger events anyway). Because UCERF3 is unsegmented, it allows more $M \sim 6.7$ events because they are consistent with data used in the inversion. The UCERF3 influence of time dependence is almost imperceptible for this main fault, except near magnitude 7.7, where the gain is below 1.0 due to the 1906 earthquake (Fig. 7).

Hayward–Rodgers Creek. The mean $M \geq 6.7$ probability for Hayward–Rodgers Creek is unchanged (0.32 in both UCERF3 and UCERF2), in spite of an increase in the probability gain (from 1.34 to 1.52) and a 24% increase in the target moment rate. These latter increases are compensated at lower magnitudes by UCERF3, including more multifault ruptures, which also manifest as an approximate doubling of probabilities above M 7.2 (Fig. 7).

Calaveras. The biggest $M \geq 6.7$ probability increase among the main faults is on the Calaveras, going from a mean of 0.08 in UCERF2 to a mean of 0.25 in UCERF3 (about a factor of 3). In fact, the UCERF2 mean is not even within the range of UCERF3 values (just below the UCERF3 minimum of 0.10). Some of this can be attributed to the probability gain

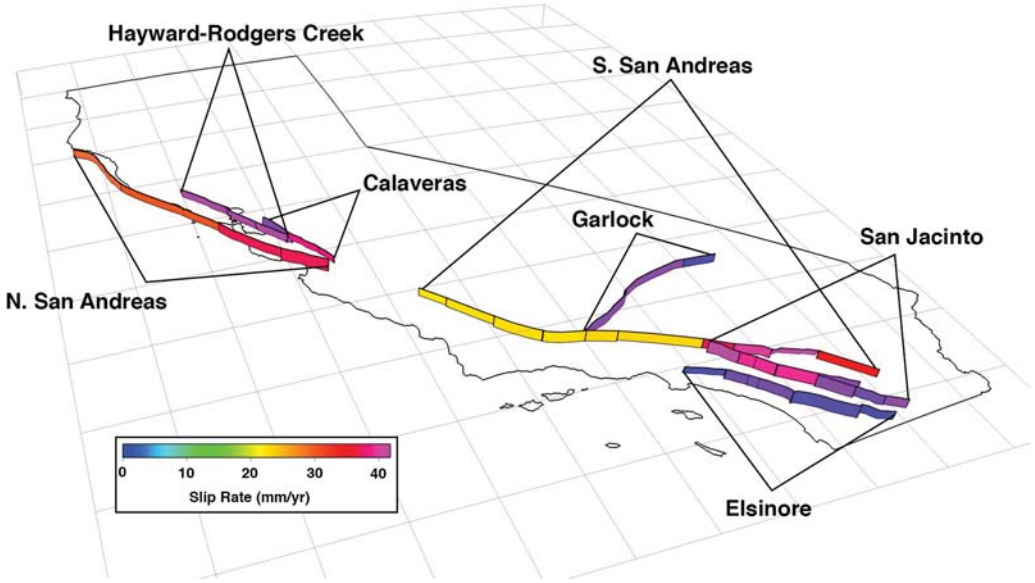

Figure 6. The main faults considered by this and previous Working Group on California Earthquake Probabilities. See Table 6 for a list of fault sections included in each. The color scale indicates the slip rate for the geologic deformation model in UCERF3-TI.

increase from 0.98 to 1.46, and some can be attributed to the 43% increase in target moment rate. However, much of the increase also comes from the Calaveras having a higher rate of participation in larger magnitude events (Fig. 7), reflecting the broader range of multifault ruptures included in UCERF3. UCERF2, on the other hand, was forced to put all moment into $M \leq \sim 7$ events, with a high fraction going into the smallest single-segment ruptures, which is why UCERF2 probabilities are actually higher than those of UCERF3 at the lowest magnitudes (Fig. 7).

San Jacinto. The biggest $M \geq 6.7$ probability decrease among main faults is on the San Jacinto, going from 0.32 in UCERF2 to 0.09 in UCERF3 (about a factor of 3 reduction). Some of this can be attributed to a gain decrease (from 1.02 to 0.83) and some to a target moment rate reduction of 23%. Figure 7 reveals a greater participation in $M \geq 7.7$ events, as defined in the long-term model, is also influential because less moment rate is available for smaller events.

Garlock. The mean $M \geq 6.7$ probability on the Garlock fault has gone from 0.06 to 0.08 between UCERF2 and UCERF3. This is consistent with a gain increase from 1.06 to 1.16 but is countered by a target moment rate reduction of 15%. Again, this is primarily due to fault-discretization issues in UCERF2 (segment lengths between 40 and 100 km), whereas UCERF3 allows shorter ruptures to the extent they are consistent with data, which increases rates near M 6.7 (Fig. 7).

Elsinore. The mean $M \geq 6.7$ probability for Elsinore has decreased from 0.11 to 0.05, mostly due to an ~43% reduction in target moment rate between UCERF2 and UCERF3, and in spite of a gain increase from 0.90 to 0.99. All segments in the UCERF2 model have lengths greater than 40 km, resulting in very few $M \leq 6.5$ earthquakes in UCERF2 (Fig. 7). UCERF3, on the other hand, allows shorter-length ruptures to the extent they are consistent with data, which takes moment rate away from $M \geq 6.7$ events.

Probabilities for Regions

Figure 8 shows cumulative magnitude–probability distributions for the following regions: the entire area (All CA), the northern half (N. CA), the southern half (S. CA), Los Angeles (LA), and San Francisco (SF). The area for each of these regions is shown in Figure 1. Probabilities for select magnitude thresholds are also listed in Table 7. Again, these probabilities reflect participation, meaning they include every event that has any part of its rupture surface inside the region, even if most is outside. This differs from the values listed in the UCERF2 documentation, where contributions were weighted by the fraction of the rupture surface inside the region (reflecting more of a nucleation probability). We prefer the definition used here because we do not want, for example, to reduce the contribution of a full South San Andreas rupture in the LA region just because it extends well to the northeast and southwest.

For All CA, probabilities remain largely unchanged between UCERF2 and UCERF3, especially given the overall epistemic uncertainties. However, probabilities in both models approach 1.0 at lower magnitudes, effectively masking any real differences. The biggest change is for $M > 8$ events, for which the mean probability has increased from 0.05 in UCERF2 to 0.07 in UCERF3. Some of this can be attributed to a gain increase from 1.06 to 1.21, but most is due to the inclusion of multifault ruptures in UCERF3, including events that rupture through the San Andreas creeping section (discussed above). Figure 8 demonstrates epistemic uncertainties for All CA have increased significantly in UCERF3 and are large compared to differences between UCERF2 and

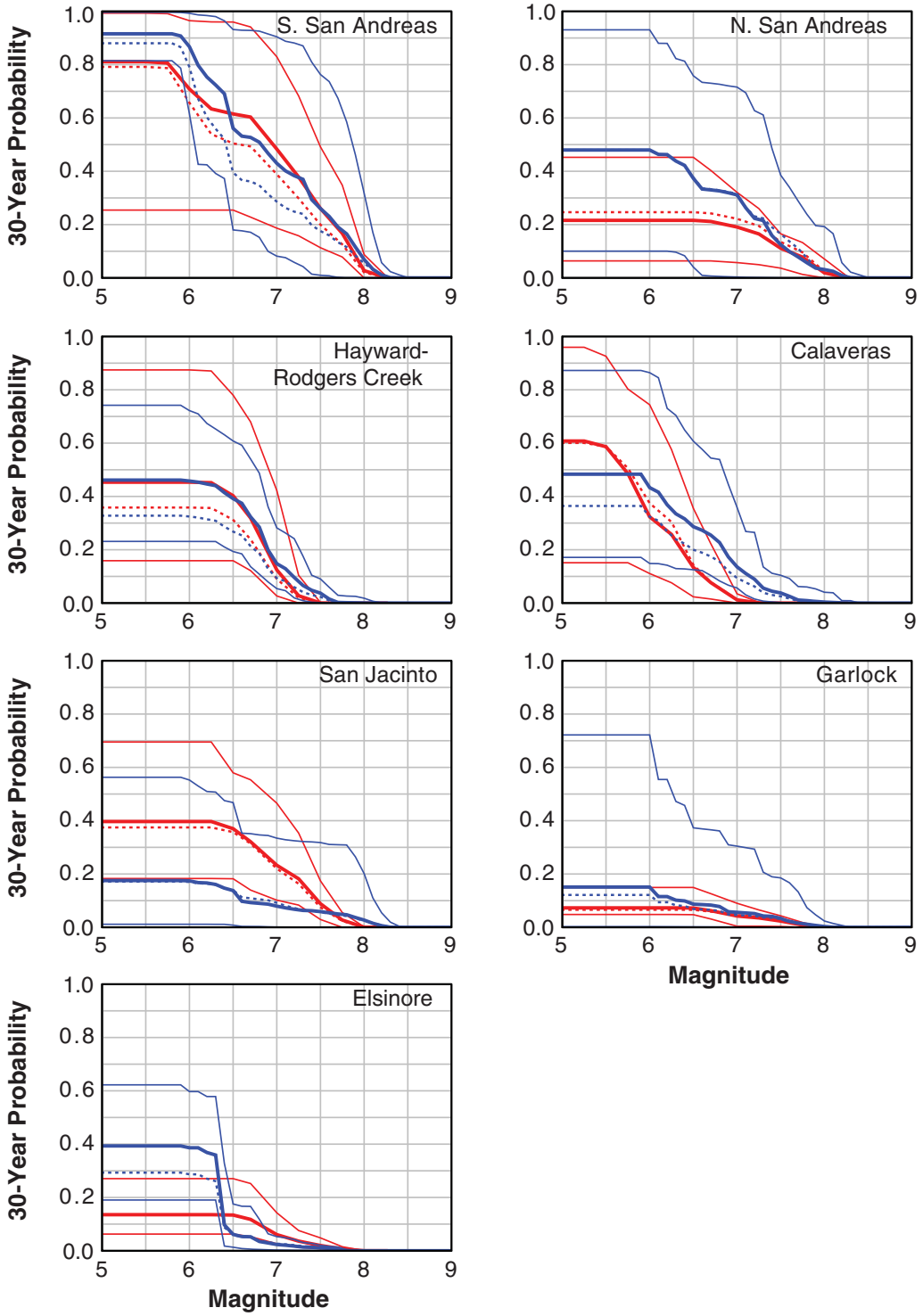

Figure 7. Thirty-year magnitude–probability distributions, representing participation probabilities as a function of magnitude, for the main faults listed in Table 5 and shown in Figure 6. UCERF3 results are shown in blue, and UCERF2 results are red. The wide lines represent branch-averaged values, the thin lines represent the minimum and maximum among branches, and the dotted lines represent time-independent model values (averaged over Poisson-model branches).

UCERF3 mean values. For example, the difference between the UCERF3 minimum and maximum value is 0.32 for $M > 8$, with the UCERF3 to UCERF2 difference being 0.02 for such magnitudes. All of these conclusions apply to the N. CA and S. CA regions as well.

The $M \geq 6.7$ probabilities for the SF area are largely unchanged, going from 0.67 in UCERF2 to 0.72 in UCERF3. Differences are greatest for $M \geq 7.5$ events, where probabilities increased by ~60% (from 0.12 to 0.20). Some of this can be attributed to a probability gain increase from 0.83

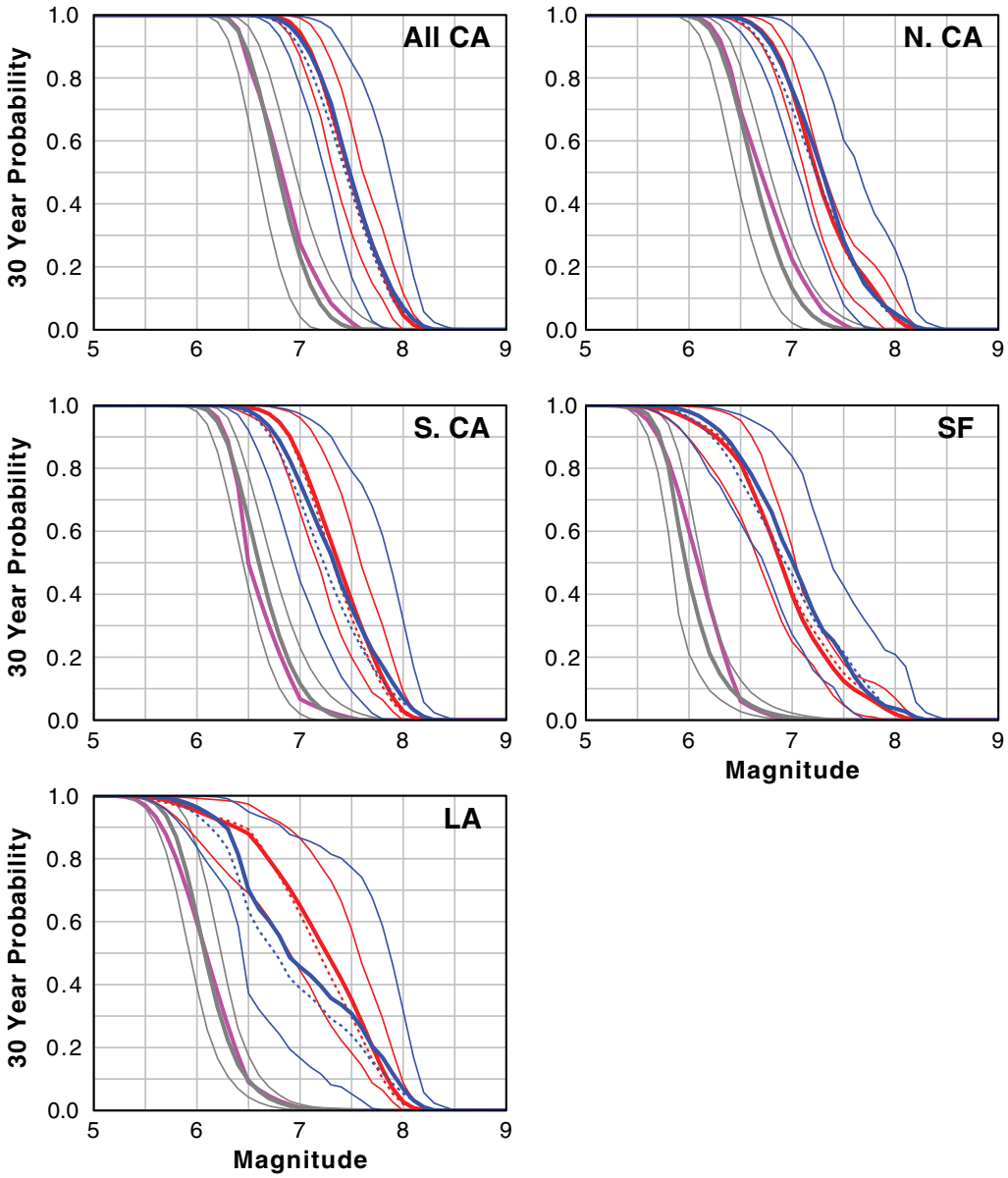

Figure 8. Thirty-year participation probabilities as a function of magnitude (magnitude–probability distributions) for the following regions: the entire California area (All CA), the northern half (N. CA), the southern half (S. CA), Los Angeles (LA), and San Francisco (SF). The area of each region is shown in Figure 1. UCERF3 results are shown in blue (based on a start year of 2014), and UCERF2 results are red (based on the start year of 2007 used in that study). The wide lines represent branch-averaged values, the thin lines represent the minimum and maximum among branches, and the dotted lines represent time-independent model values (averaged over Poisson-model branches). The gray lines represent the contribution from gridded seismicity in UCERF3 (subseismogenic and off-fault ruptures, not treated as time dependent), and the magenta line represents those from UCERF2 (where no minimum and maximum are shown because there was only one logic-tree branch).

to 0.93 and to a target moment-rate increase of 7% (see table 14 of the UCERF3-TI report). Most, however, results from a larger set of multifault ruptures being included in the UCERF3 earthquake rate model. Again, epistemic uncertainties have increased and are large compared to UCERF2–UCERF3 mean-value differences.

The LA region exhibits probability reductions of up to 30% between M 6.4 and 7.5, in spite of overall probability gain increases between UCERF2 and UCERF3. However, probabilities have increased by more than a factor of 2 for $M \geq 8$ events (from 0.03 to 0.07), with gains largely unchanged at these magnitudes. Target moment rate differences are not very influential, having gone down by 7% in this region (table 14 of the UCERF3-TI report). The probability changes, therefore, reflect the inclusion of multifault ruptures in the UCERF3 earthquake rate model, as well as a suppression of $M \sim 6.7$ events due to their being overpredicted in UCERF2. In fact, the UCERF2 to UCERF3 probability changes seen for LA are completely consistent with differences in respective long-term magnitude–frequency

Table 7
Thirty-Year Participation Probabilities for Different Regions of California

Region	Magnitude	U3 Mean	U3 Min.	U3 Max.	U3 Gain	U2 Mean	U2 Gain	U3/U2
All CA	6	1.00	1.00	1.00	1.00	1.00	1.00	1.00
	6.7	1.00	0.97	1.00	1.00	1.00	1.00	1.00
	7	0.93	0.77	1.00	1.04	0.94	1.00	0.98
	7.5	0.48	0.17	0.85	1.09	0.47	1.07	1.01
	7.7	0.27	0.03	0.71	1.08	0.27	1.09	0.98
	8	0.07	0.00	0.32	1.21	0.05	1.06	1.53
N. CA	6	1.00	1.00	1.00	1.00	1.00	1.00	1.00
	6.7	0.95	0.84	1.00	1.04	0.95	1.00	0.99
	7	0.76	0.55	0.96	1.09	0.76	1.00	1.00
	7.5	0.28	0.08	0.60	1.01	0.27	1.03	1.05
	7.7	0.15	0.01	0.45	0.94	0.17	1.05	0.87
	8	0.05	0.00	0.25	1.14	0.04	1.02	1.41
S. CA	6	1.00	1.00	1.00	1.00	1.00	1.00	1.00
	6.7	0.93	0.77	1.00	1.03	0.97	1.00	0.96
	7	0.75	0.44	0.97	1.08	0.83	1.02	0.90
	7.5	0.36	0.09	0.79	1.22	0.38	1.17	0.93
	7.7	0.22	0.02	0.68	1.29	0.21	1.23	1.06
	8	0.07	0.00	0.32	1.25	0.03	1.33	2.47
SF	6	0.98	0.89	1.00	1.02	0.96	1.00	1.02
	6.7	0.72	0.52	0.94	1.12	0.67	0.99	1.08
	7	0.51	0.27	0.84	1.09	0.40	0.97	1.27
	7.5	0.20	0.05	0.43	0.93	0.12	0.83	1.61
	7.7	0.10	0.00	0.32	0.80	0.08	0.81	1.24
	8	0.04	0.00	0.21	1.04	0.02	0.81	1.95
LA	6	0.96	0.84	1.00	1.03	0.95	1.00	1.01
	6.7	0.60	0.28	0.92	1.14	0.80	1.00	0.76
	7	0.46	0.17	0.87	1.17	0.65	1.04	0.70
	7.5	0.31	0.05	0.77	1.29	0.35	1.19	0.87
	7.7	0.20	0.01	0.68	1.33	0.20	1.25	1.01
	8	0.07	0.00	0.32	1.27	0.03	1.34	2.51

The regions are as follows: the entire California area (All CA), the northern half (N. CA), the southern half (S. CA), Los Angeles (LA), and San Francisco (SF). The area of each region is shown in Figure 1. Magnitude represents the threshold value (probabilities are for events greater than or equal to this value). U3 stands for UCERF3, based on a start year of 2014, and U2 stands for UCERF2, based on the start year of 2007 used in that study. Mean is the branch-averaged value, Min. and Max. are the extreme values among logic-tree branches, and Gain represents the average time-dependent value divided by the time-independent (Poisson) model average. U3/U2 is the ratio of UCERF3 to UCERF2 mean. All values have been rounded to the second decimal place.

distributions (fig. 26 of the UCERF3-TI report). Epistemic uncertainties are considerably wider than for the SF region and again represent an increase over those in UCERF2.

Participation Probability Maps

Figure 9 maps 30 yr $M > 6.7$ participation probabilities throughout the region for UCERF3 and UCERF2, as well as the probability gains implied by each model (results for other magnitude thresholds can be obtained from sources listed in Data and Resources). The region has been discretized into $0.1° \times 0.1°$ grid cells for these maps, and fault-based probabilities have been mapped onto the grid cells accordingly. Fault-based probabilities are spread over a slightly wider area in the UCERF3 maps, compared to those in UCERF2, which is particularly apparent for the San Andreas fault. This simply results from the fact that, in UCERF3, each fault section was assigned a polygon in order to be more explicit about the spatial area it represents (meaning any supraseismogenic rupture inside the polygon is considered an occurrence on that fault section). Fault-based probabilities are therefore spread over the grid cells that reside within the associated fault-section polygon, leading to a wider area of influence adjacent to UCERF3 faults; see Powers and Field (2013, appendix O of UCERF3-TI report) for implementation details.

Another obvious difference in the participation probability maps is the influence of UCERF2 type C zones, seen as the two large green areas in Figure 9c (one in northeastern California and the other in the Mojave Desert). These types of sources were not used in UCERF3, having been replaced by newly added faults and improved deformation models.

Of more relevance to the influence of elastic rebound are the probability gain maps (Fig. 9b,d). Areas with gains below 1.0 in UCERF3 represent faults that have recently ruptured. Gains below 1.0 in UCERF2, on the other hand, generally represent the influence of the empirical model, which has not been included in UCERF3 for reasons discussed in the Introduction. Perhaps the most important difference,

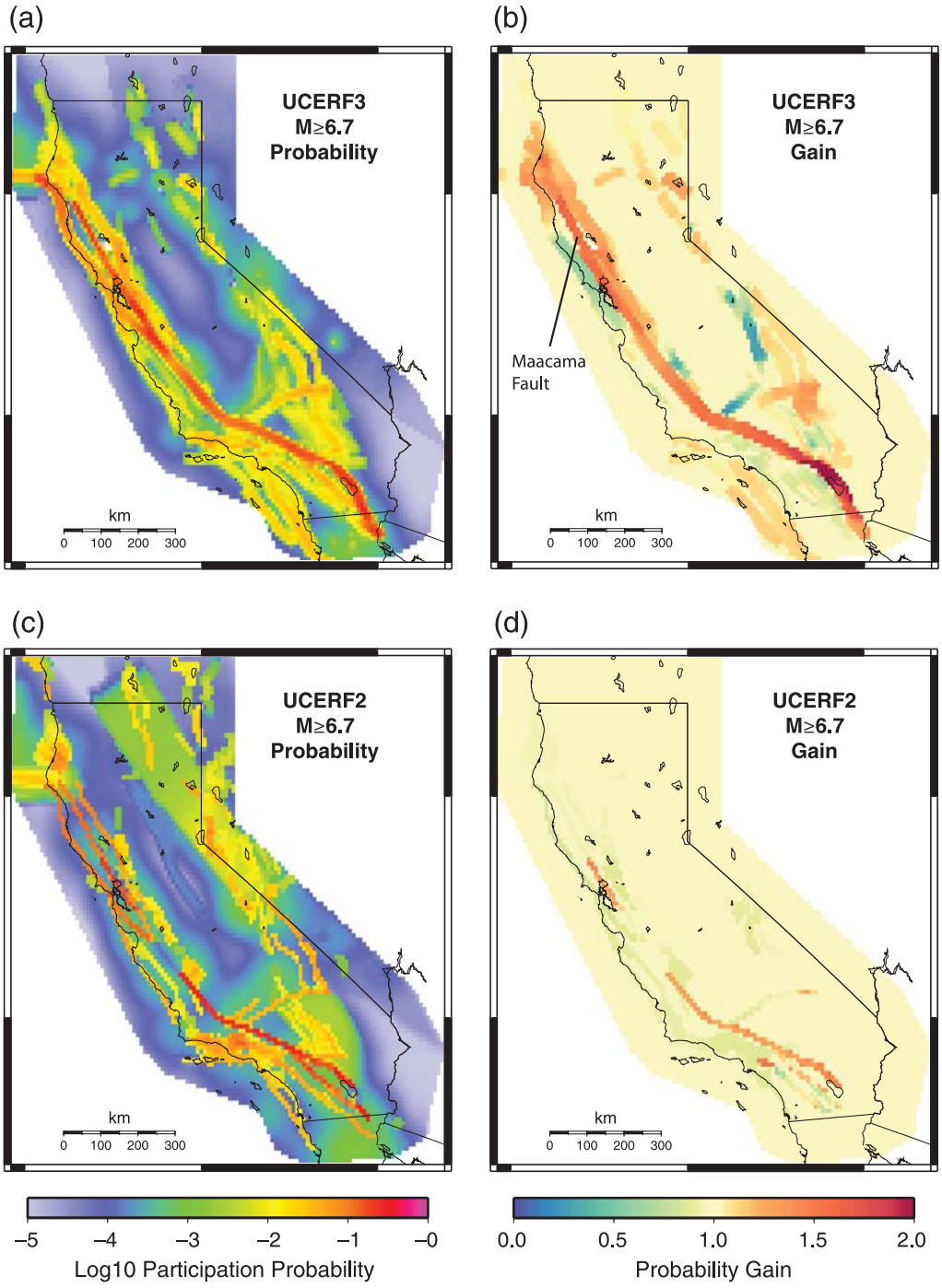

Figure 9. Thirty-year $M \geq 6.7$ participation probability and implied gains throughout the region, where fault-based probabilities have been aggregated onto $0.1° \times 0.1°$ grid cells, and subseismogenic and off-fault ruptures are included (as time-independent sources). (a) Branch-averaged probabilities for the UCERF3 time-dependent model. (b) Probability gains implied by UCERF3, obtained by dividing the time-dependent probability averages by those obtained from the time-independent (Poisson) model branches. (c) Same as (a) but for UCERF2. (d) Same as (b) but for UCERF2.

however, is that UCERF3 exhibits larger probability gains and over larger areas. Much of this can be attributed to the influence of the historic open interval, which was not used in UCERF2, and produces significant probability gains on high-rate faults that have not had a recent event. A good example of this is Maacama 2011 CFM, which made the top-10 list in Table 5 and can be seen as the prominent red lineament in northern California (shown in Fig. 9b).

For faults where elastic-rebound probabilities were computed in both models, the gains in UCERF3 are generally higher than those in UCERF2. For example, San Andreas (Coachella) rev had a gain of 1.43 in UCERF2 but now has

a gain of 1.86 according to UCERF3. The total weight applied to elastic-rebound models in UCERF2 was 0.63 (when considering both the unsegmented branch and the empirical model option), whereas the total weight for elastic-rebound branches in UCERF3 is 0.80 (Table 1). Were we to reduce the UCERF3 value to that applied in UCERF2, the San Andreas (Coachella) rev gain would be 1.46, which is very close to the UCERF2 value of 1.43. Therefore, the higher gains on UCERF3 faults can also be attributed to an effective increase in the weight applied to the elastic-rebound model.

Figure 10 shows equivalent 30 year participation maps for $M \geq 7.7$ events, for which conclusions are generally similar to those drawn for the $M \geq 6.7$ maps (Fig. 9). A much greater fraction of the region participates in $M \geq 7.7$ events in UCERF3, compared to UCERF2, but this is a manifestation of earthquake rate model differences rather than elastic rebound.

Hazard Map Ratios

As noted, each of the metrics presented above has limitations with respect to inferring practical implications. Here, we address the question of how the time dependence might influence building codes, which have traditionally considered the ground motions that have some chance of being exceeded in 50 years, as determined via probabilistic seismic-hazard analysis. The USGS National Seismic Hazard Mapping Program generates a variety of probabilistic maps for this purpose (e.g., Algermissen *et al.*, 1982; Frankel *et al.*, 1996, 2002; Petersen *et al.*, 2008), and these have been updated recently for official release in 2014 (Petersen *et al.*, 2014). For California, the new maps utilize the UCERF3 time-independent (Poisson) model.

Figure 11 compares the UCERF3 and UCERF2 time-dependent models in terms of the time-dependent gain for peak ground acceleration (PGA) with a 2% chance of being exceeded in 50 years (time-dependent maps divided by time-independent maps). In general, the trends in Figure 11 follow those seen in the participation probability maps (Figs. 9 and 10), including the differences between UCERF2 and UCERF3. An obvious exception is in southeast California, where there is a wide area of gain not seen in the participation probability maps. This represents the influence of the San Andreas fault, which dominates the hazard in this region because the area lacks more local influences. This high gain does not necessarily reflect a high hazard, however, as the absolute difference in PGA levels can be quite small and perhaps inconsequential from an engineering design perspective. Nevertheless, this reflects the potential long geographical reach of hazard influences, which are not reflected in the evaluation metrics presented above. For example, it has been shown that earthquakes on the San Andreas (Coachella) rev can efficiently channel long-period ground motions into the greater LA basin (e.g., Olsen *et al.*, 2006), so a hazard map for such shaking might show consequential gains in this highly populated area. This also exemplifies how conclusions will depend on the exact hazard metric. Plots for other ground-motion parameters can be obtained from sources in Data and Resources.

Sensitivity Tests

Influence of Logic-Tree Branches

For a few metrics, we explore the range of values implied by the 5760 logic-tree branches, and we quantify which epistemic uncertainties are most influential. We consider 30 yr $M \geq 6.7$ subsection participation probabilities first, for which branch-averaged values were discussed previously (and plotted in Fig. 5a). Figure 12 shows the range of probabilities, normalized by the mean on each subsection, implied by the various logic-tree branches, and including all subsections. The spread of values is also quantified by the standard deviation listed next to each histogram, representing how each branch contributes to the overall epistemic uncertainty. The deformation models (alternative slip rates) produce the widest range of values, with the scaling relationships coming in second, and the probability models coming in third. All of the remaining branches have considerably less influence, on average, although the relative influence of each varies significantly by fault.

Figure 13 shows a map view of the relative influence of each deformation model on 30 yr $M \geq 6.7$ subsection probabilities. For example, the Geologic and Zeng models give relatively high values on the northern San Andreas fault, whereas the other two models produce relatively low values (by definition, the values shown among the four models at a point on a fault sum to 1.0). Likewise, Figures 14 and 15 show equivalent influence maps for the scaling-relationship and probability-model branches, respectively. As expected, the deformation models produce the widest range of values overall, but the relative influence of each branch varies considerably across the fault system. Plots for the other branches, as well as for other magnitude thresholds, and for a 5 year forecast, can be obtained from sources in Data and Resources.

Turning to the two most populated areas of California, Figures 16 and 17 show branch sensitivities for 30 yr $M \geq 6.7$ probabilities in the SF and LA regions, respectively. Here, the histograms have the same total shape for each branch because there is only one probability, as opposed to a probability for each subsection in Figure 12. The contribution from each branch option is plotted with a different color, along with a vertical bar representing the mean for that branch. The horizontal distance between the vertical bars therefore indicates overall sensitivity to that logic-tree branch. For SF, the influences in descending order are (1) total $M \geq 5$ event rate; (2) probability models; (3) scaling relationships; (4) deformation models; (5) M_{max} off fault; (6) off-fault spatial seis PDF; (7) slip along rupture models; and (8) fault models.

For LA, the influential logic-tree branches in descending order are (1) total $M \geq 5$ event rate; (2) probability models; (3) scaling relationships and off-fault spatial seis PDF (about equal); (4) deformation models and M_{max} off fault (about equal); and (5) slip along rupture models and fault models (about equal).

The different logic-tree-branch influences in these regions highlight the spatial variability of such inferences.

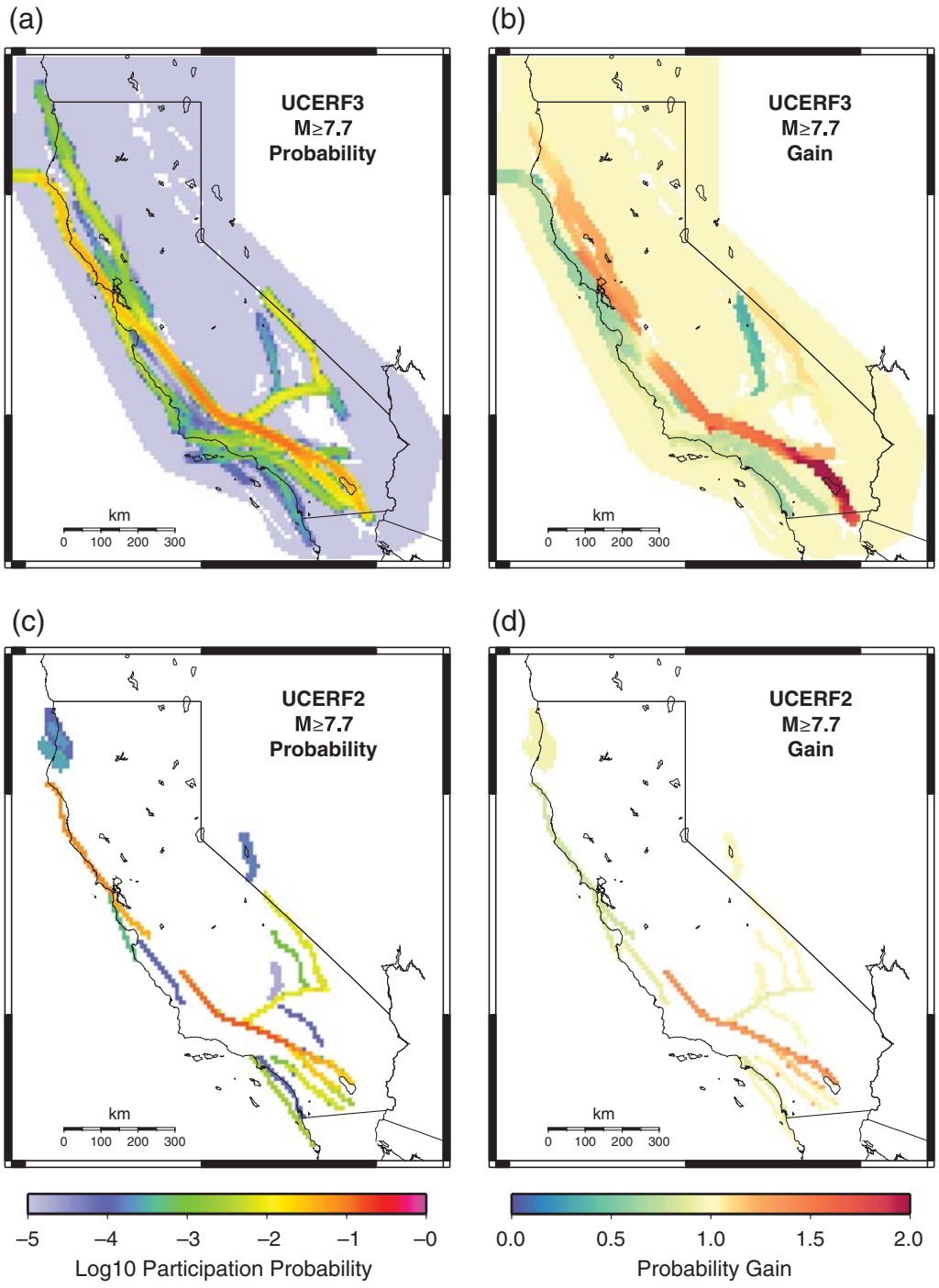

Figure 10. Same as Figure 9, but for $M \geq 7.7$ probabilities.

Conclusions also depend on the chosen evaluation metric, which in this case was 30 yr $M \geq 6.7$ participation probabilities. It is obviously beyond the scope of this article to evaluate every metric of potential interest.

Influence of Historic Open Interval Test

For reasons discussed above, we assumed a historic open interval based on the year 1875. To quantify sensitivity of this decision, Figure 18 maps relative 30 yr $M \geq 6.7$ probabilities for three alternative values, based on 1850, 1900, and 2014 (the latter representing zero open interval). Probabilities obtained for 1850 and 1900 show negligible differences compared to the epistemic uncertainties shown in Figures 13, 14, and 15. The differences between 1875 and 2014 are more important, especially for the higher slip-rate faults, which is why we have chosen to account for the historic open interval. Accounting for the historic open interval increases probability gains relative to UCERF2.

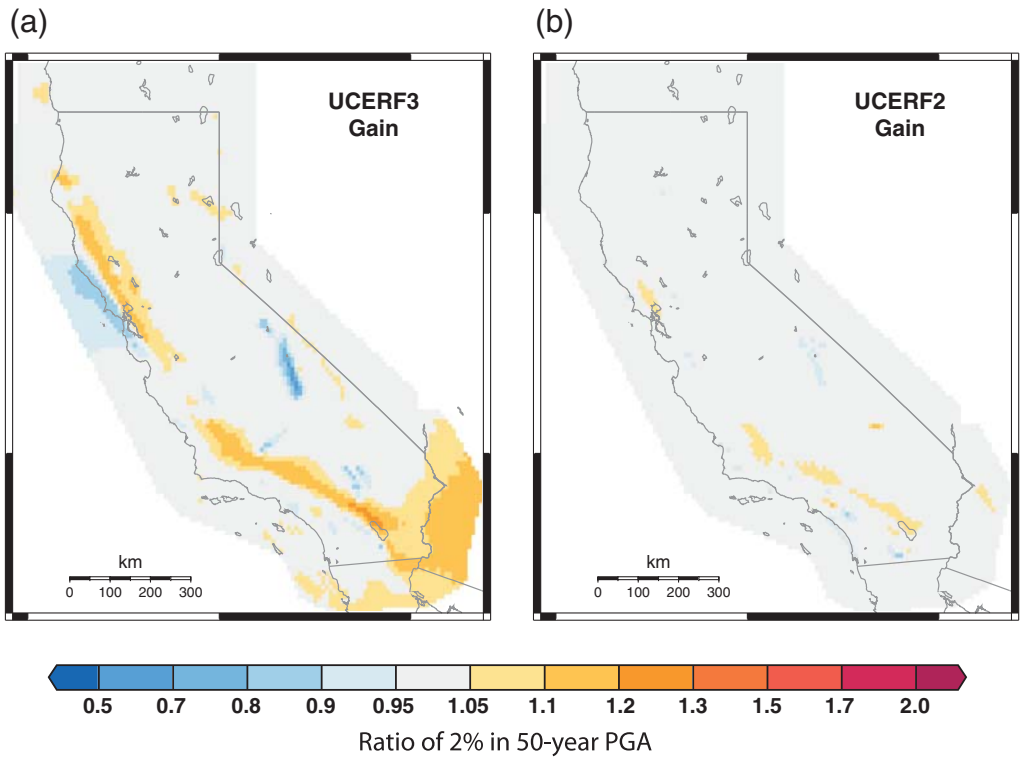

Figure 11. Time-dependent gain maps for the peak ground acceleration that has a 2% chance of being exceeded in 50 years, obtained by dividing time-dependent maps by time-independent maps (averaged over all relevant logic-tree branches in both UCERF2 and UCERF3). The ground-motion prediction equations utilized are the same as those applied in the 2014 update of the U.S. Geological Survey National Seismic Hazard Maps (Petersen *et al.*, 2014).

Influence of Different Averaging Approaches

As discussed in Field (2015), there are different ways of averaging over subsections in computing both the conditional recurrence interval (μ_r^{cond}) and average time since last event for each rupture. The formulation presented above averages section recurrence intervals in computing μ_r^{cond}, whereas we could alternatively compute this as one over the average of section rates. Likewise, we could average the date of the last event on each subsection, rather than averaging the normalized time since the last event, as specified above. Extensive testing has been conducted to evaluate the viability and influence of each option, and the formulation presented here represents our current preference, although two alternatives remain viable. For UCERF3, the differences are negligible when the date of the last event is known on all fault sections, with some marginally important difference appearing when accounting for unknown last-event dates. The approach here gives probabilities that are in between the two viable alternatives, so adding an equally weighted logic-tree branch would have relatively little influence on average metrics; for example, the biggest difference in $M \geq 6.7$ 30 yr probabilities among all subsections is 0.01, and this value is just 2% of the difference between minimum and maximum probabilities. Stated another way, the influence of a branch for the different averaging methods would be on a par with that of fault models in Figure 12.

Discussion

The UCERF3 time-dependent forecast appears to be a reasonable representation of elastic-rebound theory. It implies reduced probabilities, or low gains, where events have recently occurred (e.g., North San Andreas, Owens Valley), and elevated probability gains where faults have a higher normalized time since the last event (e.g., San Andreas [Coachella] rev, San Andreas [San Bernardino S]). It also produces higher gains on faults that have short recurrence intervals relative to the historic open interval (e.g., Maacama 2011 CFM). Perhaps more surprising is the influence that highly probable faults have on neighbors with which they tend to corupture (e.g., the influence of San Andreas [Coachella] rev on Eureka Peak), revealing a potentially important consequence of fault interconnectivity.

Differences between UCERF3 and UCERF2

In general, differences between UCERF3 and UCERF2 probabilities arise mostly from changes in the long-term earthquake rate model. For example, Calaveras exhibits the largest 30 yr $M \geq 6.7$ probability increase among the main faults (a factor of ~3), only about a third of which can be attributed to time-dependent-model differences. The rest is due to increased average slip rate and a change in the shape of the long-term magnitude–frequency distribution. In UCERF2, the Calaveras fault was restricted to mostly $M \leq 6.5$ ruptures,

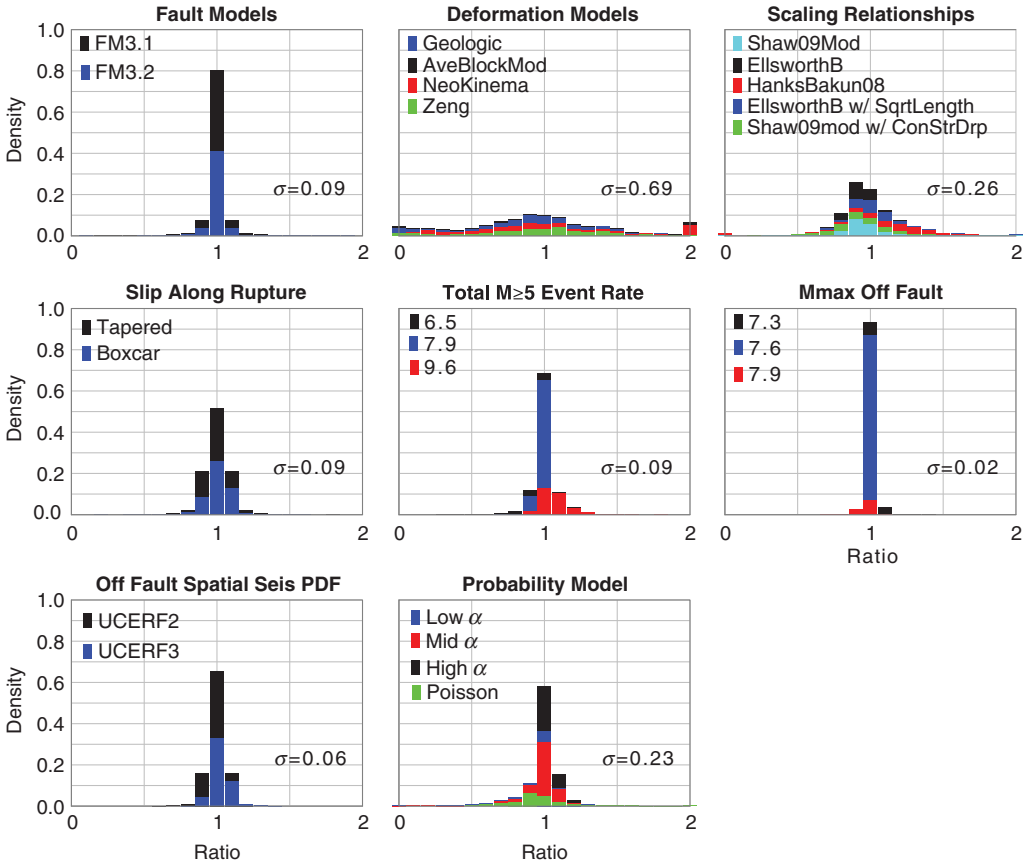

Figure 12. The influence of each logic-tree branch (Fig. 3) on 30 yr $M \geq 6.7$ subsection probabilities. For example, the upper left histogram plots the range of values observed among the two fault model branches (FM3.1 in black versus FM3.2 in blue), where the bars for the former are stacked on top of those of the latter (added together, rather than overlaying the respective histograms). The histograms include the values for every subsection, and each is normalized by the mean on that subsection. Actual branch weights are accounted for in these plots. The standard deviation (σ) for each histogram is also listed, indicating the spread of values, or implied epistemic uncertainty, for each logic-tree branch.

whereas the inclusion of multifault ruptures in UCERF3 has increased the rate of $M \geq 6.7$ events.

The addition of multifault ruptures has had the opposite effect on $M \geq 6.7$ probabilities for the San Jacinto fault, which exhibits the largest decrease among the main faults (about a factor of 3). Here, multifault ruptures have increased the rate of $M \geq 7.7$ earthquakes, effectively stealing moment rate away from smaller sized events, which has lowered the probability of $M \geq 6.7$ events. Also influential is a drop in average slip rate and a lower probability gain. Finally, 30 yr probabilities for $M \geq 6.7$ earthquakes increased on both the North San Andreas and Garlock main faults, simply because the UCERF2 segments were too long to produce an adequate set of such shorter-length events.

Statewide, event probabilities remain largely unchanged between UCERF2 and UCERF3, except for an increase at $M \geq 8.0$, due primarily to the inclusion of multifault ruptures in the UCERF3 earthquake rate model (including full San Andreas fault ruptures). The same goes for the San Francisco region, where the inclusion of multifault ruptures has increased $M \geq 7.5$ probabilities by 60%. Large event probabilities have also increased in the LA area (e.g., by a factor of ~2.5 at $M \geq 8$), but they have also decreased by up to 30% between M 6.4 and 7.5. These changes reflect not only the inclusion of multifault ruptures, but also the deliberate suppression of $M \sim 6.7$ events, via the UCERF3 inversion, to avoid UCERF2's overprediction of such events.

These examples highlight the range of factors influencing UCERF2 to UCERF3 probability changes, with most being related to the long-term earthquake rate model. Stated another way, most of the differences between UCERF3 and UCERF2 are greater than the range of probability gains implied by each model. Furthermore, most of the differences are small compared to overall epistemic uncertainties, which have increased significantly in UCERF3. The above examples also demonstrate that focusing on any single evaluation metric, like $M \geq 6.7$ probabilities, can be misleading in terms of potential hazard implications.

With respect to time-dependent-model differences, the biggest influences are accounting for the historic open interval in UCERF3, which only serves to increase probabilities relative to Poisson, and an effective increase in the weight applied to elastic-rebound models. As noted above, this weight was 0.63 in UCERF2, with the rest going into the Poisson and empirical models, whereas the total weight on elastic rebound in UCERF3 is 0.80. This 27% weight

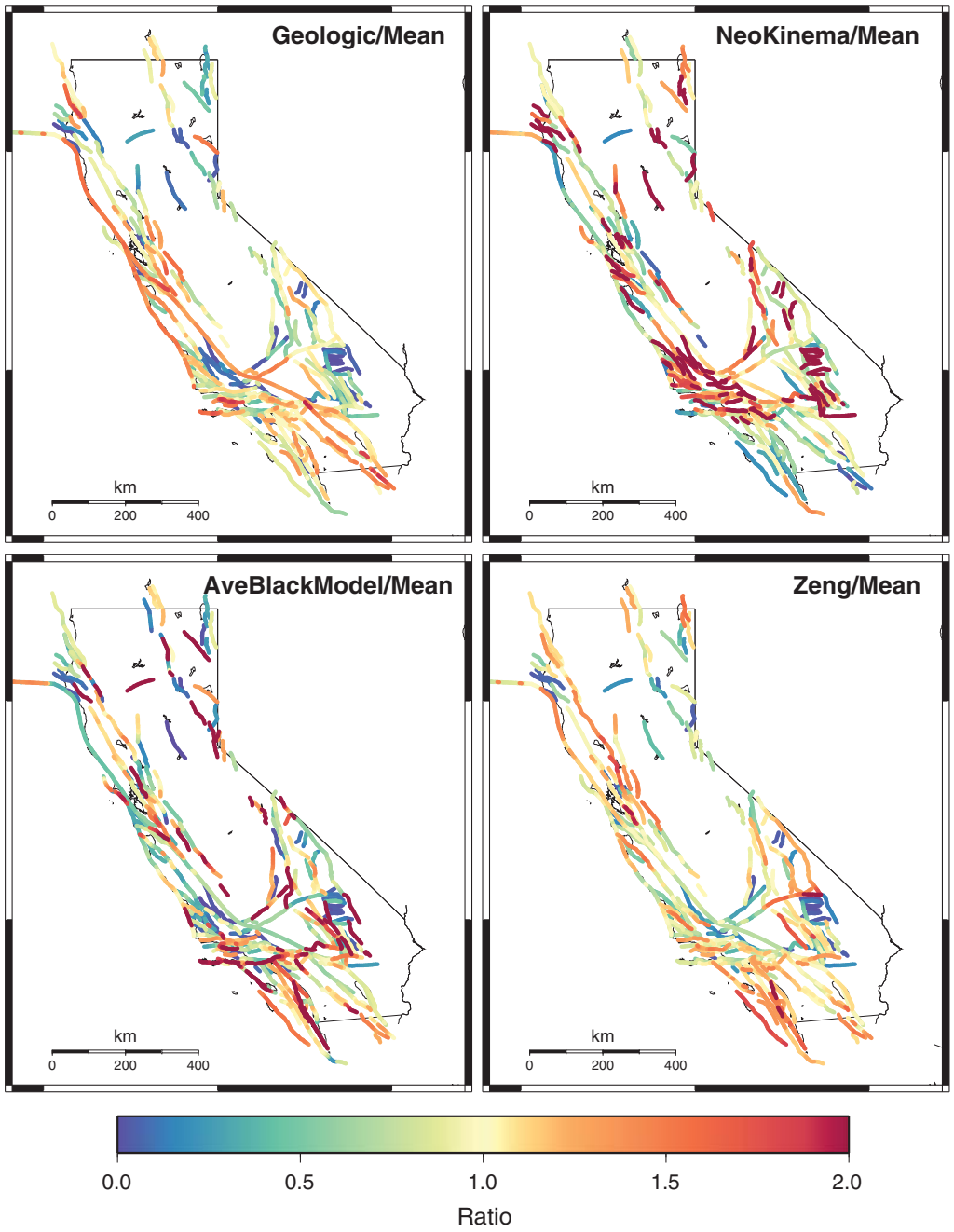

Figure 13. Average 30 yr $M \geq 6.7$ subsection probabilities for each deformation model branch, separately, normalized by the overall mean on each subsection. In other words, summing values across the four different maps equals 1.0, revealing the overall influence of each branch (assuming each is weighted equally here). Such plots for other logic-tree branches are available from sources in Data and Resources.

increase, together with the influence of the historic open interval, explains why the UCERF3 gain map has more red areas than that of UCERF2 (Fig. 9).

Influence of Logic-Tree Branches

For all subsections taken together, the alternative deformation models (slip rates) produce the widest range of probabilities, with the scaling relationships coming in second, and the probability models coming in third. The relative influence of logic-tree branches varies significantly by fault and by region. For example, the total, regional $M \geq 5$ event rate has the largest influence on $M \geq 6.7$ probabilities in both the SF and LA regions, with probability models coming in second and scaling relationships coming in third. Apparently slip rates are relatively well resolved in these areas, or tradeoffs between neighboring faults are canceling out.

Again, such inferences depend on the evaluation metric. For example, deformation models are presumably more influential than total $M \geq 5$ event rates at higher magnitudes (e.g.,

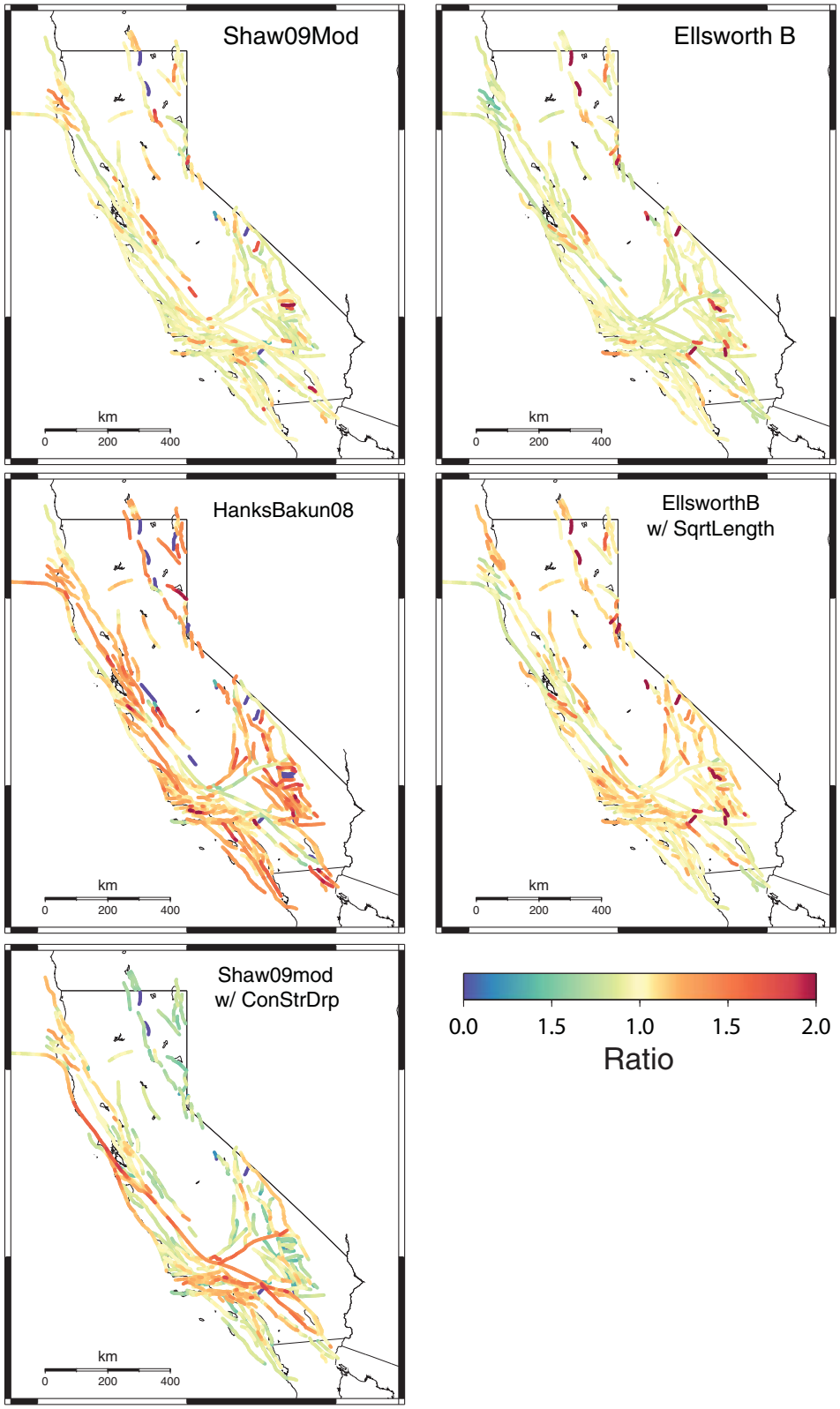

Figure 14. Same as Figure 13 but for the scaling relationship branch options. Equivalent plots for other logic-tree branches are available from sources in Data and Resources. (Models are referenced in full in Fig. 3.)

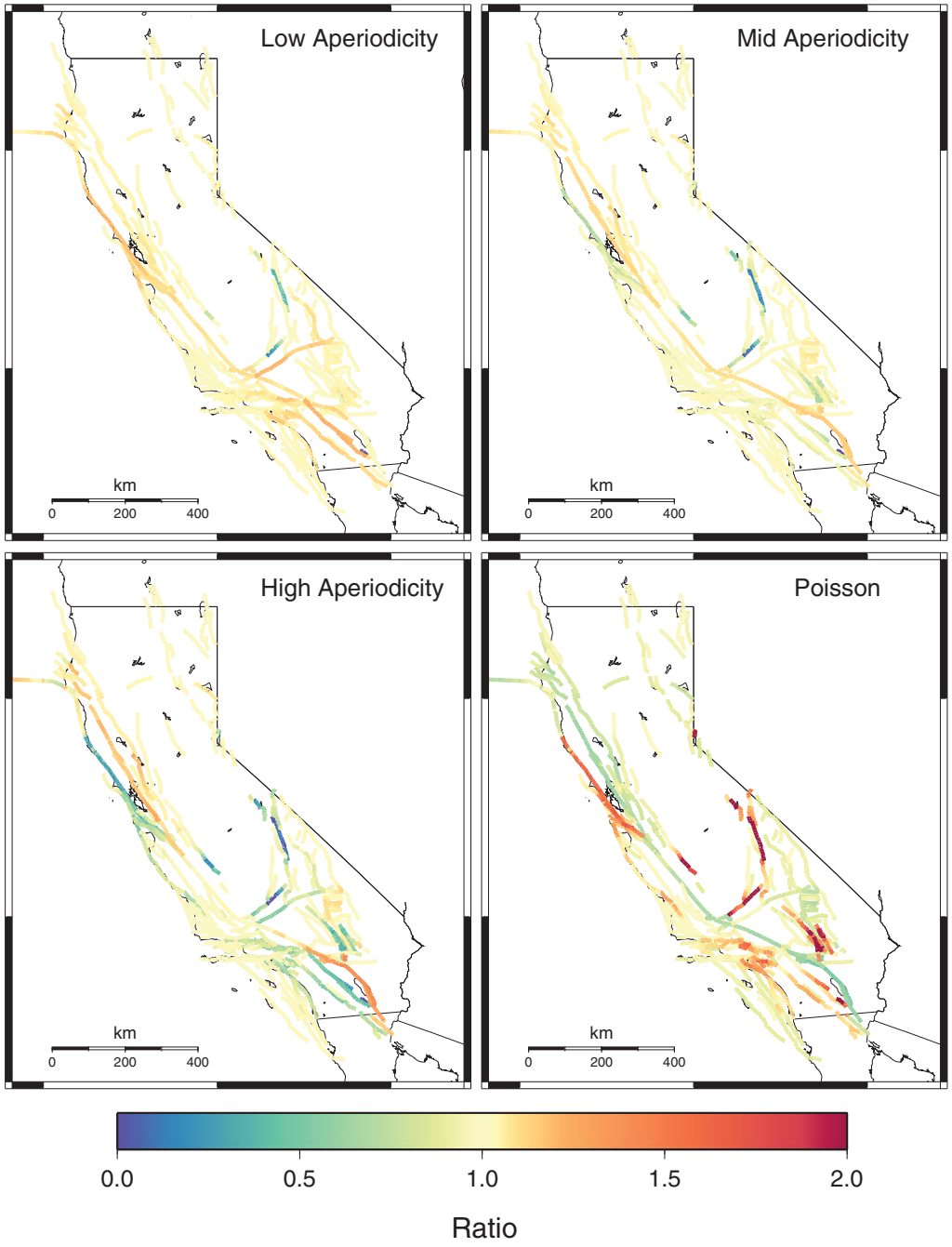

Figure 15. Same as Figure 13, but for the different probability model options. Equivalent plots for other logic-tree branches are available from sources in Data and Resources.

$M > 7.7$). Evaluations of logic-tree sensitivity, as well as influences on UCERF2 to UCERF3 differences, need to be made on a case-by-case basis. The conclusions will certainly differ depending on whether one is producing statewide portfolio loss estimates, designing a single family dwelling in Sacramento, retrofitting the San Francisco Bay bridge, or putting a pipeline across the San Andreas fault. We obviously cannot quantify branch influences for every situation here, but we do provide computer code that can aid such case-by-case assessments (see Data and Resources).

The weights assigned to logic-tree branches might also warrant adjustment depending on study details. For example, preliminary implementations of our spatiotemporal clustering model imply incompatibility with a Poisson model, as mentioned in the Introduction, so probability model weights might need to be adjusted in an operational earthquake forecast. Other situations in which adjustments might be warranted, including site-specific studies, are discussed in the UCERF3-TI report with respect to the time-independent model.

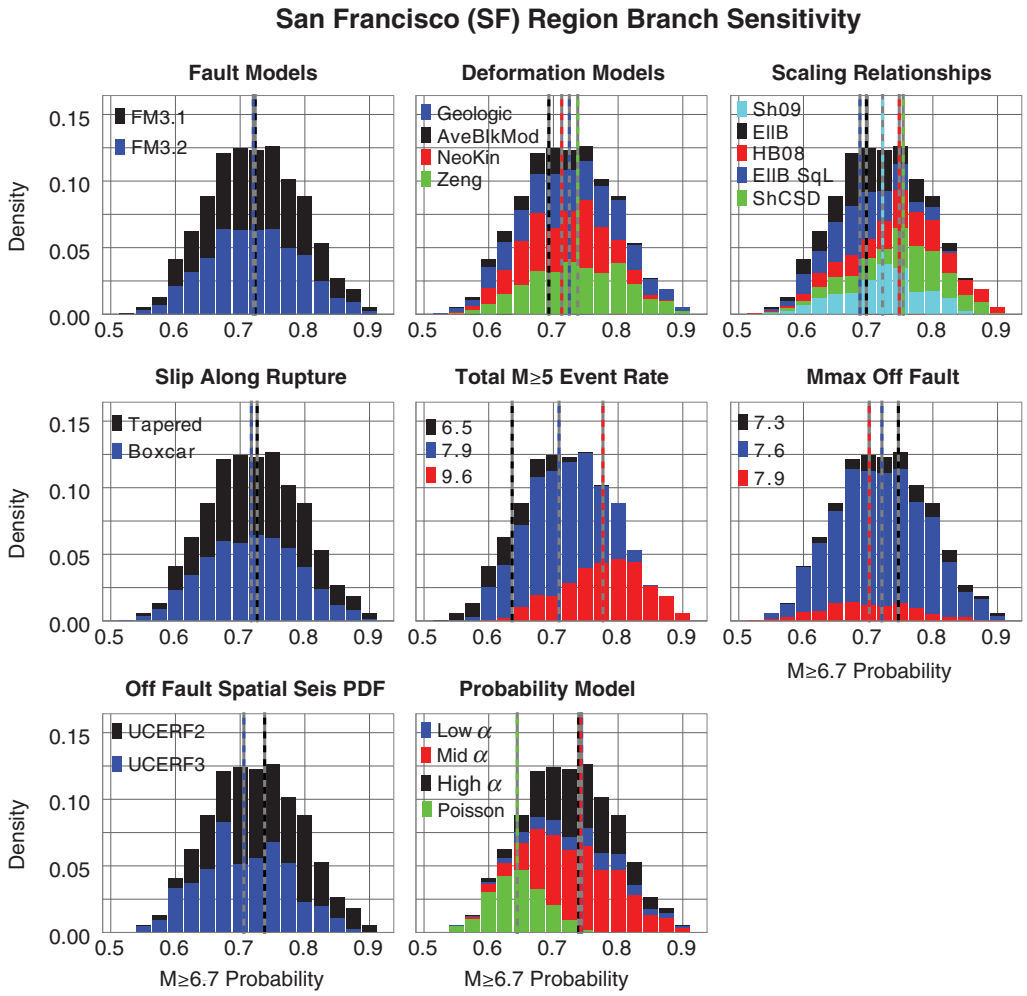

Figure 16. The influence of each logic-tree branch on 30 yr $M \geq 6.7$ probabilities for the San Francisco (SF) region, the area of which is shown in Figure 1. For example, the black area in the upper left histogram shows the range of values for the FM3.1 fault model option, whereas the blue area represents those of the alternative logic-tree branch (FM3.2). The histograms are stacked on top of each other (added together rather than overlaid). Branch weights are accounted for here, as reflected by the relative area occupied by each color. The colored, vertical dashed bars show mean values for each branch, with greater distance between those of alternative branch options implying greater epistemic uncertainty. (Models are referenced in full in Fig. 3.)

Model Testability

Our model assumes elastic-rebound effects exist in the real earthquake system, because the infrequency of supraseismogenic earthquakes has exacerbated definitive tests. Fortunately, the methodology as formulated here is testable. It predicts that the recurrence interval of each supraseismogenic earthquake can be estimated by averaging the long-term recurrence intervals along the rupture surface and that event-to-event deviations from this expected value can be represented with a classic renewal model. There is no need to wait for multiple events along the same stretch of fault. As long as estimates of long-term recurrence intervals exist along the observed rupture, any large earthquake can potentially represent a data point in testing the model.

This test also avoids challenges associated with inferring recurrence-interval distributions from paleoseismic data. As discussed by Field (2015), there is no reason to expect the distribution at a point on a fault (e.g., as seen in a trench) to look like a classic renewal model, unless one assumes strict segmentation. This and other interpretive issues, such as missed events, will therefore need to be considered when inferring elastic-rebound predictability from paleoseismic data.

Of course we must continue to rely on paleoseismology to provide reliable mean recurrence-interval estimates, as these constrain the earthquake rate model, which then gets used to define the expected recurrence intervals in our elastic-rebound model. However, we may need to avoid assumptions about the underlying distribution, as addressed by Parsons (2012). The point here is that deeper interpretations of paleoseismic data are not required to test our time-dependent model (although they would not hurt). Collecting an adequate observational dataset may not be trivial, but it is theoretically feasible.

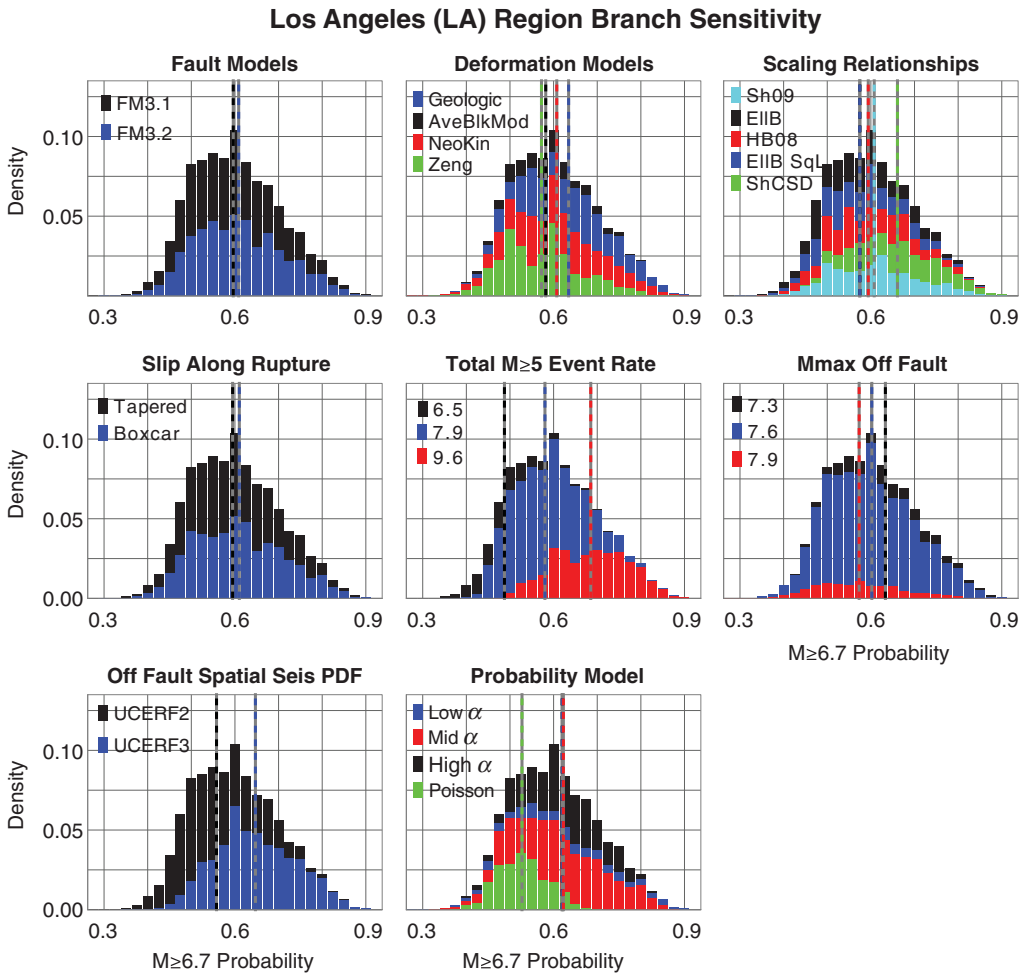

Figure 17. Same as Figure 16, but for the Los Angeles (LA) region plotted in Figure 1. (Models are referenced in full in Figure 3.)

Model Limitations and Future Improvements

All forecast models represent an approximation of the system. Several limitations of the time-independent model are discussed in the UCERF3-TI report, so we focus here on those associated with the time-dependent probability models. In addition to assuming that elastic-rebound effects exist in nature, we also effectively assume that other time-dependent processes are negligible. We know for certain that spatiotemporal effects exist in the form of aftershocks and otherwise triggered events, which we hope to add to UCERF3 soon. However, and as mentioned in the Introduction, there may be other processes as well, such as supercycles, mode switching, or whatever might be causing the rate changes that motivated the empirical model of previous WGCEPs (assuming they are not an artifact of something else).

There are also potential issues with respect to our elastic-rebound implementation. The high probability gain on the Maacama 2011 CFM fault section exemplifies one potential problem. As noted, this high gain stems from the historic open interval being a significant fraction of the long-term recurrence interval along the fault. However, it is completely unaffected by the great 1906 event on the neighboring San Andreas fault, and it is possible that the latter could have cast a probabilistic shadow (e.g., Harris and Simpson, 1998) on this and other neighboring faults. In fact, such shadowing effects may also be underestimated by the back-slip model assumptions utilized in current physics-based simulators, which otherwise include stress transfer effects (e.g., Tullis *et al.*, 2012).

Another issue, discussed in the Methodology section above, is that our model gives a zero probability for supra-seismogenic ruptures that completely overlap the surface of a recent, larger event. Although observations of such events are at least rare, their occurrence seems feasible from a dynamic rupture perspective. Including the Poisson branch was our only means of hedging on this question. This is not to say our model has zero overlap with recently ruptured fault areas, as the rupture probability effectively declines gradually as the degree of overlap increases. In fact, when a branching fault is encountered, our model will give a higher probability for rupturing the option with a higher normalized time since the last event, which effectively conforms to the explanation given by Schwartz *et al.* (2012) on why the 2002 Denali earthquake branched onto the Totschunda fault.

As touched on by Field (2015), details of the elastic-rebound implementation, including assumed aperiodicity,

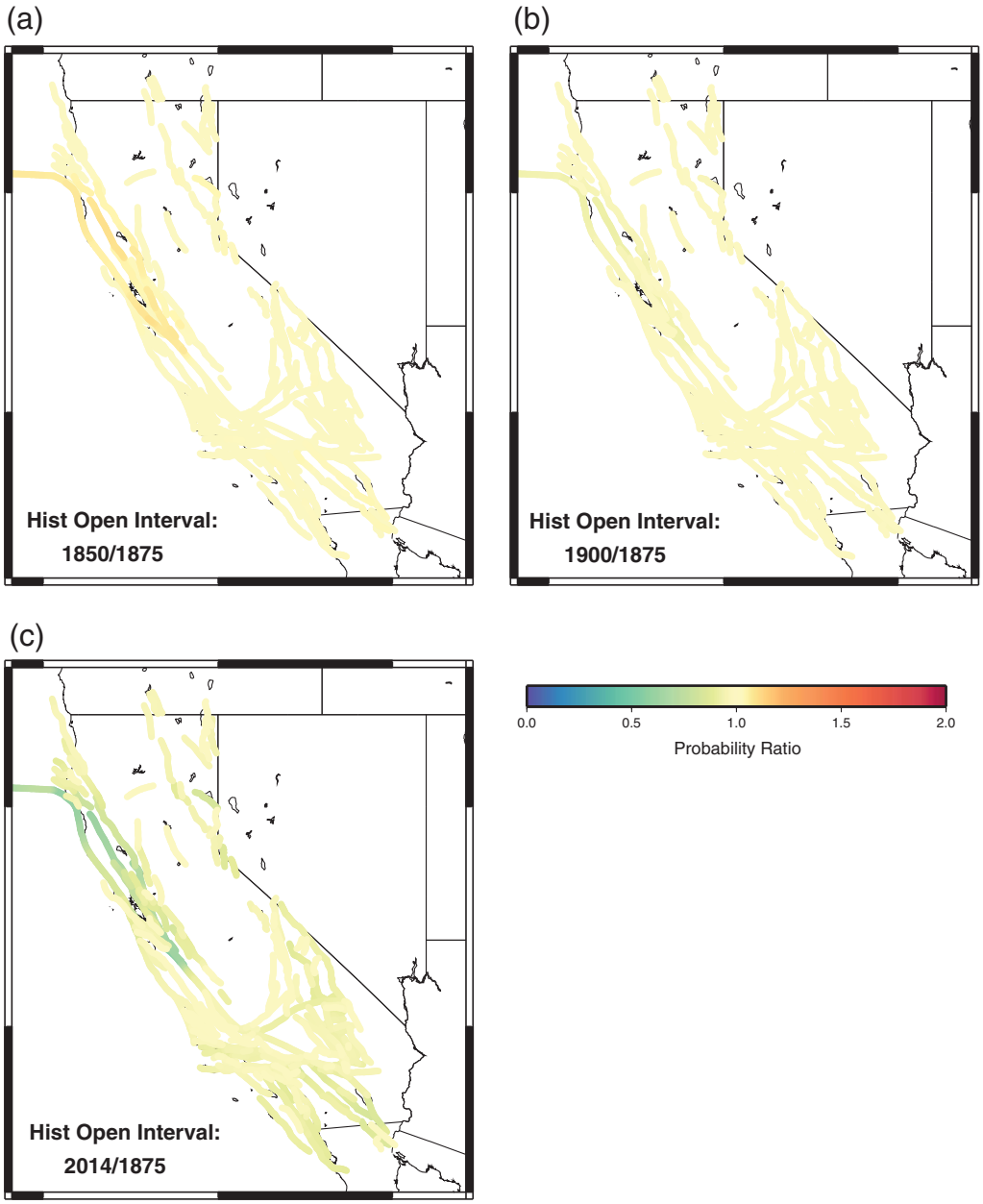

Figure 18. Ratio of 30 yr $M \geq 6.7$ subsection probabilities obtained for alternative historic open intervals, divided by those obtained for 1875 (the value assumed in UCERF3): (a) 1850; (b) 1900; and (c) 2014 (zero historic open interval since the forecast starts at 2014).

have a significant influence on the degree of overlap among adjacent ruptures. Furthermore, this overlap will only increase when spatiotemporal clustering is added, because aftershock statistics will have a preference for triggering a large event on adjacent fault sections, rather than triggering a more distant fault. Having better observational constraints on spatial overlap could therefore provide a powerful means of testing all types of forecast models.

The UCERF3-TI report discusses a number of ways the logic-tree branches could be expanded with respect to the time-independent model. Possible expansions with respect to the UCERF3 probability models include: (1) alternative renewal models (besides BPT); (2) alternative interpretations of date-of-last event data, especially with respect to the lateral extent of events (which are currently minimized with respect to paleoseismic constraints); (3) alternative historic open interval assumptions, including region- or fault-specific values; and (4) alternative approaches for averaging renewal model parameters across the subsections utilized by each rupture. Sensitivity tests suggest that adding these branches would produce only a minor influence on results (e.g., well below 10%), at least for most metrics and in most areas. We therefore believe it will be more productive to address other shortcomings, such as the lack of spatiotemporal clustering.

Adding more logic-tree branches will only serve to expand the epistemic uncertainties, which have already

increased considerably between UCERF2 and UCERF3. Unfortunately, this means we have yet to reach the tipping point where incremental model improvements start reducing epistemic uncertainties. That we are making this conclusion for one of the most data-rich and highly scrutinized areas on Earth is telling with respect to the scientific maturity of earthquake forecasting. It is also disconcerting with respect to the implied unknowns in other regions.

A final consideration is the 10% overprediction of long-term rates implied by Monte Carlo simulations, as discussed in the Methodology section. This bias is relatively small compared to both the overall probability gains and epistemic uncertainties but could nevertheless be corrected by lowering all probabilities by 10%. For example, correcting the 30 yr $M \geq 6.7$ probabilities on the San Andreas (Coachella) rev fault section would produce the following (corrected values in parentheses):

- mean: 0.27 (0.24)
- minimum: 0.07 (0.06)
- maximum: 0.60 (0.54)
- gain: 1.86 (1.67)

The difference here between corrected and uncorrected mean values (0.03) is only about 6% of the difference between the minimum and maximum values. Given this relatively small influence, we have chosen not to make such corrections here. We also note that previous models suffer such biases as well; they just were not recognized at the time. Users are certainly free to make their own judgments with respect to these corrections. However, if one deems the differences important, then surely consideration of the full logic tree would be in order, as applying mean values might not be appropriate given overall uncertainties.

Conclusions

Relaxing segmentation and including multifault ruptures presented significant challenges with respect to representing elastic-rebound theory in UCERF3. This led to the development of a new methodology, which is more conceptually self-consistent than the previous approach and less biased in terms of reproducing long-term rates in Monte Carlo simulations. The methodology is also consistent with the elastic-rebound predictability seen in physics-based simulators, it can accommodate magnitude-dependent aperiodicity, and it can account for the historic open interval on faults that lack date-of-last-event data, all of which represent advantages over the previous approach. The model is also inherently more testable.

The new methodology is far from perfect, however. It assumes elastic rebound dominates other known and suspected processes that are not included in the model. There are also a number of ways the logic tree could be expanded to represent other epistemic uncertainties. Nevertheless, we believe the model currently represents the best available science with respect to quantifying the potential influence of elastic rebound. Full implications of the model will need to be studied on a case-by-case basis, and such analyses might warrant adjustment of the logic-tree branch weights assigned here. Given the time-dependent nature of the model, results should also be recomputed with an alternative start time if appropriate and as new constraints are obtained for the time since last event on faults.

Data and Resources

Higher-resolution versions of figures, results for other evaluation metrics, and additional files needed to implement the model (e.g., probability of each rupture) are available at http://www.WGCEP.org/UCERF3 (last accessed January 2015).

All calculations were made using OpenSHA (http://www.OpenSHA.org; last accessed October 2014; Field *et al.*, 2003), which in turn utilizes Generic Mapping Tools (http://gmt.soest.hawaii.edu; last accessed January 2012) and JFreeChart (http://www.jfree.org/jfreechart/; last accessed March 2012) for making plots.

Acknowledgments

We are very grateful for the thoughtful and helpful reviews provided by our participatory Scientific Review Panel, chaired by William Ellsworth, and with the following other participants: Duncan Agnew, Ramón Arrowsmith, Yehuda Ben-Zion, Greg Beroza, Mike Blanpied, James Dieterich, Arthur Frankel, Sue Hough, Warner Marzocchi, Hamid Haddadi, Rick Schoenberg, and David Schwartz. This article also benefited greatly from extensive comments provided by two anonymous *BSSA* reviewers. Our Management Oversight Committee (Thomas Jordan [Chair], Tom Brocher, Jill McCarthy, and Chris Wills) helped with project guidance and requisite resources, and Tran Huynh and John McRaney provided logistics and subcontracting assistance. The Southern California Earthquake Center (SCEC) Community Modeling Environment, University of Southern California Center for High-Performance Computing and Communications, and the Texas Advanced Computing Center provided access to the high-performance computing. This study was sponsored by the California Earthquake Authority, the U.S. Geological Survey (USGS), the California Geological Survey, and the SCEC. SCEC is supported in part by the National Science Foundation under Cooperative Agreement EAR-1033462 and by the USGS under Cooperative Agreement G12AC20038. The SCEC Contribution Number for this paper is 2066. Any use of trade, product, or firm names is for descriptive purposes only and does not imply endorsement by the U.S. Government.

References

Algermissen, S. T., D. M. Perkins, P. C. Thenhaus, S. L. Hanson, and B. l. Bender (1982). Probabilistic estimates of maximum acceleration and velocity in rock in the contiguous United States, *U.S. Geol. Surv. Open-File Rept. 82-1033*.

Ben-Zion, Y. (2008). Collective behavior of earthquakes and faults: Continuum-discrete transitions, evolutionary changes and corresponding dynamic regimes, *Rev. Geophys.* **46,** RG4006, doi: 10.1029/2008RG000260.

Ben-Zion, Y., K. Dahmen, V. Lyakhovsky, D. Ertas, and A. Agnon (1999). Self-driven mode switching of earthquake activity on a fault system, *Earth Planet. Sci. Lett.* **172,** 11–21.

Biasi, G. P., and R. J. Weldon (2009). San Andreas fault rupture scenarios from multiple paleoseismic records: Stringing pearls, *Bull. Seismol. Soc. Am.* **99,** 471–498, doi: 10.1785/0120080287.

Dahmen, K., D. Ertas, and Y. Ben-Zion (1998). Gutenberg–Richter and characteristic earthquake behavior in simple mean-field models of heterogeneous faults, *Phys. Rev. E* **58,** 1494–1501.

Dolan, J. F., D. D. Bowman, and C. G. Sammis (2007). Long-range and long-term fault interactions in southern California, *Geology* **35,** 855–858.

Felzer, K. R. (2007). Empirical estimation of regional time variation in seismicity, *U.S. Geol. Surv. Open-File Rept. 2007-1437-M*.

Felzer, K. R. (2013). Appendix Q: The empirical model, *U.S. Geol. Surv. Open-File Rept. 2013-1165-Q and California Geol. Surv. Special Rept. 228-Q*.

Field, E. H. (2007). Overview of the working group for the development of Regional Earthquake Likelihood Models (RELM), *Seismol. Res. Lett.* **78,** 7–16.

Field, E. H. (2011). Aftershock statistics constitute the strongest evidence for elastic rebound in large earthquakes? *2011 Fall Meeting of the American Geophysical Union*, San Francisco, California, 5–9 December 2011.

Field, E. H. (2012). Aftershock statistics constitute the strongest evidence for elastic relaxation in large earthquakes—Take 2, *2012 Meeting of the Seismological Society of America*, San Diego, California, 17–19 April 2012.

Field, E. H. (2015). Computing elastic-rebound-motivated earthquake probabilities in unsegmented fault models: A new methodology supported by physics-based simulators, *Bull. Seismol. Soc. Am.* **105,** doi: 10.1785/0120140094.

Field, E. H., and T. H. Jordan (2015). Time-dependent renewal-model probabilities when date of last earthquake is unknown, *Bull. Seismol. Soc. Am.* **105,** 459–463, doi: 10.1785/0120140096.

Field, E. H., R. J. Arrowsmith, G. P. Biasi, P. Bird, T. E. Dawson, K. R. Felzer, D. D. Jackson, K. M. Johnson, T. H. Jordan, C. Madden, A. J. Michael, K. R. Milner, M. T. Page, T. Parsons, P. M. Powers, B. E. Shaw, W. R. Thatcher, R. J. Weldon, and Y. Zeng (2014). Uniform California Earthquake Rupture Forecast, version 3 (UCERF3): The time-independent model, *Bull. Seismol. Soc. Am.* **104,** 1122–1180, doi: 10.1785/0120130164.

Field, E. H., G. P. Biasi, P. Bird, T. E. Dawson, K. R. Felzer, D. D. Jackson, K. M. Johnson, T. H. Jordan, C. Madden, A. J. Michael, K. R. Milner, M. T. Page, T. Parsons, P. M. Powers, B. E. Shaw, W. R. Thatcher, R. J. Weldon, and Y. Zeng (2013). Uniform California Earthquake Rupture Forecast, version 3 (UCERF3): The time-independent model, *U.S. Geol. Surv. Open-File Rept. 2013–1165 and California Geol. Surv. Special Rept. 228*, http://pubs.usgs.gov/of/2013/1165/ (last accessed January 2015).

Field, E. H., T. E. Dawson, K. R. Felzer, A. D. Frankel, V. Gupta, T. H. Jordan, T. Parsons, M. D. Petersen, R. S. Stein, R. J. Weldon II, and C. J. Wills (2009). Uniform California earthquake rupture forecast, version 2 (UCERF 2), *Bull. Seismol. Soc. Am.* **99,** 2053–2107, doi: 10.1785/0120080049.

Field, E. H., T. H. Jordan, and C. A. Cornell (2003). OpenSHA: A developing community-modeling environment for seismic hazard analysis, *Seismol. Res. Lett.* **74,** 406–419.

Frankel, A., C. Mueller, T. Barnhard, D. Perkins, E. Leyendecker, N. Dickman, S. Hanson, and M. Hopper (1996). National seismic-hazard maps: Documentation June 1996, *U.S. Geol. Surv. Open-File Rept. 96-532*.

Frankel, A. D., M. D. Petersen, C. S. Mueller, K. M. Haller, R. L. Wheeler, E. V. Leyendecker, R. L. Wesson, S. C. Harmsen, C. H. Cramer, D. M. Perkins, and K. S. Rukstales (2002). Documentation for the 2002 update of the National Seismic Hazard Map, *U.S. Geol. Surv. Open-File Rept. 2002-420*.

Goldfinger, C., Y. Ikeda, R. S. Yeats, and J. Ren (2013). Superquakes and supercycles, *Seismol. Res. Lett.* **84,** doi: 10.1785/0220110135.

Grant, L. B., and K. Sieh (1994). Paleoseismic evidence of clustered earthquakes on the San Andreas fault in Carrizo Plain, California, *J. Geophys. Res.* **99,** 6819–6841.

Hanks, T. C., and W. H. Bakun (2008). M-log$A$ observations of recent large earthquakes, *Bull. Seismol. Soc. Am.* **98,** 490–494.

Harris, R. A., and R. W. Simpson (1998). Suppression of large earthquakes by stress shadows: A comparison of Coulomb and rate-and-state failure, *J. Geophys. Res.* **103,** 24,439–24,451.

Holmes, R. R., Jr., L. M. Jones, J. C. Eidenshink, J. W. Godt, S. H. Kirby, J. J. Love, C. A. Neal, N. G. Plant, M. L. Plunkett, C. S. Weaver, A. Wein, and S. C. Perry (2013). U.S. Geological Survey natural hazards science strategy: Promoting the safety, security, and economic well-being of the nation, *U.S. Geol. Surv. Circular 1383–F*, 79 pp.

Hough, S. E. (1994). Southern surface rupture associated with the M 7.3 Landers, California earthquake, *Bull. Seismol. Soc. Am.* **84,** 817–825.

Jennings, C. W., and W. A. Bryant (2010). Fault activity map of California: California Geological Survey Geologic Data Map No. 6.

Jordan, T. H., and L. M. Jones (2010). Operational earthquake forecasting: Some thoughts on why and how, *Seismol. Res. Lett.* **81,** no. 4, 571–574.

Jordan, T. H., Y.-T. Chen, P. Gasparini, R. Madariaga, I. Main, W. Marzocchi, G. Papadopoulos, G. Sobolev, K. Yamaoka, and J. Zschau (2011). Operational earthquake forecasting: State of knowledge and guidelines for implementation, Final Report of the International Commission on Earthquake Forecasting for Civil Protection, *Ann. Geophys.* **54,** no. 4, 315–391, doi: 10.4401/ag-5350.

Kaiser, A., C. Holden, J. Beavan, D. Beetham, R. Benites, A. Celentano, D. Collett, J. Cousins, M. Cubrinovski, G. Dellow, P. Denys, E. Fielding, B. Fry, M. Gerstenberger, R. Landgridge, C. Massey, M. Motagh, N. Pondard, G. McVerry, J. Ristau, M. Stirling, J. Thomas, S. R. Uma, and J. Zhao (2012), The M_w 6.2 Christchurch earthquake of February, 2011: Preliminary report, *New Zeal. J. Geol. Geophys.* **55,** 67–90, doi: 10.1080/00288306.2011.641182.

Madden, C., D. E. Haddad, J. B. Salisbury, O. Zielke, J. R. Arrowsmith, R. J. Weldon II, and J. Colunga (2013). Appendix R: Compilation of slip in the last event data and analysis of last event, repeated slip, and average displacement for recent and prehistoric ruptures, *U.S. Geol. Surv. Open-File Rept. 2013-1165-R and California Geol. Surv. Special Rept. 228-R*.

Matthews, M. V., W. L. Ellsworth, and P. A. Reasenberg (2002). A Brownian model for recurrent earthquakes, *Bull. Seismol. Soc. Am.* **92,** 2233–2250.

Milner, K. R., M. T. Page, E. H. Field, T. Parsons, G. P. Biasi, and B. E. Shaw (2013). Appendix T: Defining the inversion rupture set via plausibility filters, *U.S. Geol. Surv. Open-File Rept. 2013-1165-T and California Geol. Surv. Special Rept. 228-T*.

Ogata, Y. (1988). Statistical models of point occurrences and residual analysis for point processes, *J. Am. Stat. Assoc.* **83,** 9–27.

Olsen, K. B., S. M. Day, J. B. Minster, Y. Cui, A. Chourasia, M. Faerman, R. Moore, P. Maechling, and T. Jordan (2006). Strong shaking in Los Angeles expected from southern San Andreas earthquake, *Geophys. Res. Lett.* **33,** L07305, doi: 10.1029/2005GL025472.

Page, M. T., E. H. Field, K. R. Milner, and P. M. Powers (2013). Appendix N: Grand inversion implementation and testing, *U.S. Geol. Surv. Open-File Rept. 2013-1165-N and California Geol. Surv. Special Rept. 228-N*.

Page, M. T., E. H. Field, K. R. Milner, and P. M. Powers (2014). The UCERF3 grand inversion: Solving for the long-term rate of ruptures in a fault system, *Bull. Seismol. Soc. Am.* **104,** 1181–1204, doi: 10.1785/0120130180.

Parsons, T. (2012). Paleoseismic interevent times interpreted for an unsegmented earthquake rupture forecast, *Geophys. Res. Lett.* **39,** L13302, doi: 10.1029/2012GL052275.

Petersen, M. D., A. D. Frankel, S. C. Harmsen, C. S. Mueller, K. M. Haller, R. L. Wheeler, R. L. Wesson, Y. Zeng, O. S. Boyd, D. M. Perkins, N. Luco, E. H. Field, C. J. Wills, and K. S. Rukstales (2008). Documentation for the 2008 update of the United States National Seismic Hazard Maps, *U.S. Geol. Surv. Open-File Rept. 2008-1128*.

Petersen, M. D., M. P. Moschetti, P. M. Powers, C. S. Mueller, K. M. Haller, A.D. Frankel, Y. Zeng, S. Rezaeian, S. C. Harmsen, O. S. Boyd, N. Field, R. Chen, K. S. Rukstales, N. Luco, R. L. Wheeler, R. A. Williams, and A. H. Olsen (2014). Documentation for the 2014 update of the United States national seismic hazard maps, *U.S. Geol. Surv. Open-File Rept. 2014-1091*, 243 pp., 10.3133/ofr20141091.

Porter, K. A., E. H. Field, and K. Milner (2012). Trimming the UCERF 2 hazard logic tree, *Seismol. Res. Lett.* **83,** 815–828, doi: 10.1785/0220120012.

Powers, P. M., and E. H. Field (2013). Appendix O: Gridded seismicity sources, *U.S. Geol. Surv. Open-File Rept. 2013-1165-O and California Geol. Surv. Special Rept. 228-O*.

Reid, H. F. (1911). The elastic-rebound theory of earthquakes, *Univ. Calif. Pub. Bull. Dept. Geol. Sci.* **6,** 413–444.

Rockwell, T. K., T. E. Dawson, J. Young, and G. Seitz (2014). A 21 event, 4,000-year history of surface ruptures in the Anza seismic gap, San Jacinto fault: Implications for long-term earthquake production on a major plate boundary fault, *Pure Appl. Geophys.* doi: 10.1007/s00024-014-0955-z.

Schwartz, D. P., P. J. Haeussler, G. G. Seitz, and T. E. Dawson (2012). Why the 2002 Denali fault rupture propagated onto the Totschunda fault: Implications for fault branching and seismic hazards, *J. Geophys. Res.* **117,** doi: 10.1029/2011JB008918.

Schwartz, D. P., J. J. Lienkaemper, S. Hecker, K. I. Kelson, T. E. Fumal, J. N. Baldwin, G. G. Seitz, and T. M. Niemi (2014). The earthquake cycle in the San Francisco Bay region: A.D. 1600–2012, *Bull. Seismol. Soc. Am.* **104,** 1299–1328, doi: 10.1785/0120120322.

Shaw, B. E (2013a). Earthquake surface slip-length data is fit by constant stress drop and is useful for seismic hazard analysis, *Bull. Seismol. Soc. Am.* **103,** 876–893, doi: 10.1785/0120110258.

Shaw, B. E (2013b). Appendix E: Evaluation of magnitude-scaling relationships and depth of rupture: Recommendation for UCERF3, *U.S. Geol. Surv. Open-File Rept. 2013-1165-E* and *California Geol. Surv. Special Rept. 228-E.*

Tullis, T. E., K. Richards-Dinger, M. Barall, J. H. Dieterich, E. H. Field, E. M. Heien, L. H. Kellogg, F. F. Pollitz, J. B. Rundle, M. K. Sachs, D. L. Turcotte, S. N. Ward, and M. B. Yikilmaz (2012). Comparison among observations and earthquake simulator results for the allcal2 California fault model, *Seismol. Res. Lett.* **83,** 994–1006.

Weldon, R., K. Scharer, T. Fumal, and G. Biasi (2004). Wrightwood and the earthquake cycle: What a long recurrence record tells us about how faults work, *GSA Today* **14,** 4–10.

Working Group on California Earthquake Probabilities (WGCEP) (1988). Probabilities of large earthquakes occurring in California on the San Andreas fault, *U.S. Geol. Surv. Open-File Rept.*, 62 pp.

Working Group on California Earthquake Probabilities (WGCEP) (1990). Probabilities of large earthquakes in the San Francisco Bay region, California, *U.S. Geol. Surv. Circular*, 51 pp.

Working Group on California Earthquake Probabilities (WGCEP) (1995). Seismic hazards in southern California: Probable earthquakes, 1994–2024, *Bull. Seismol. Soc. Am.* **85,** 379–439.

Working Group on California Earthquake Probabilities (WGCEP) (2003). Earthquake probabilities in the San Francisco Bay region: 2002–2031, *U.S. Geol. Surv. Open-File Rept. 2003-214.*

Working Group on California Earthquake Probabilities (WGCEP) (2007). The Uniform California earthquake rupture forecast, version 2 (UCERF x2), *U.S. Geol. Surv. Open-File Rept. 2007-1437.*

Zaliapin, I., V. Keilis-Borok, and M. Ghil (2003). A Boolean delay model of colliding cascades. I: Multiple seismic regimes, *J. Stat. Phys.* **111,** 815–837.

U.S. Geological Survey
Denver Federal Center
P.O. Box 25046, MS 966
Denver, Colorado 80225-0046
(E.H.F., P.M.P., Y.Z.)

University of Nevada Reno
Nevada Seismological Laboratory MS-174
1664 N. Virginia Street
Reno, Nevada 89557
(G.P.B.)

Department of Earth, Planetary, and Space Sciences
University of California
Los Angeles, California 90095-1567
(P.B., D.D.J.)

California Geological Survey
345 Middlefield Road MS 520
Menlo Park, California 94025
(T.E.D.)

U.S. Geological Survey
525 S. Wilson Avenue
Pasadena, California 91106
(K.R.F., M.T.P.)

Department of Geological Sciences
Indiana University
1001 E. 10th Street
Bloomington, Indiana 47405
(K.M.J.)

University of Southern California
Southern California Earthquake Center
3651 Trousdale Parkway No. 169
Los Angeles, California 90089-0742
(T.H.J., K.R.M.)

College of Earth, Ocean, and Atmospheric Sciences
Oregon State University
104 CEOAS Administration Building
Corvallis, Oregon 97331-5503
(C.M.)

U.S. Geological Survey MS 977
345 Middlefield Road
Menlo Park, California 94025
(A.J.M., W.R.T.)

U.S. Geological Survey MS 999
345 Middlefield Road
Menlo Park, California 94025
(T.P.)

Lamont Doherty Earth Observatory
Columbia University
Palisades, New York 10964
(B.E.S.)

Department of Geological Sciences
University of Oregon
Eugene, Oregon 97403-1272
(R.J.W.)

Manuscript received 4 April 2014;
Published Online 10 March 2015